A Bayesian INLA-SPDE Approach to Spatio-Temporal Point-Grid Fusion with Change-of-Support and Misaligned Covariates

Weiyue Zheng, Andrew Elliott, Claire Miller, Marian Scott

School of Mathematics and Statistics, University of Glasgow, University Avenue, Glasgow, G128QQ, Scotland, United Kingdom

Abstract

We propose a spatio-temporal data-fusion framework for point data and gridded data with variables observed on different spatial supports. A latent Gaussian field with a Matérn-SPDE prior provides a continuous space representation, while source-specific observation operators map observations to both point measurements and gridded averages, addressing change-of-support and covariate misalignment. Additionally incorporating temporal dependence enables prediction at unknown locations and time points. Inference and prediction are performed using the Integrated Nested Laplace Approximation and the Stochastic Partial Differential Equations approach, which delivers fast computation with uncertainty quantification. Our contributions are: a hierarchical model that jointly fuses multiple data sources of the same variable under different spatial and temporal resolutions and measurement errors, and a practical implementation that incorporates misaligned covariates via the same data fusion framework allowing differing covariate supports. We demonstrate the utility of this framework via simulations calibrated to realistic sensor densities and spatial coverage. Using the simulation framework, we explore the stability and performance of the approach with respect to the number of time points and data/covariate availability, demonstrating gains over single-source models through point and gridded data fusion. We apply our framework to soil moisture mapping in the Elliot Water catchment (Angus, Scotland). We fuse in-situ sensor data with aligned and misaligned covariates, satellite data and elevation data to produce daily high resolution maps with uncertainty.

Keywords: data fusion, misalignment covariate, Integrated Nested Laplace Approximation (INLA), Stochastic partial differential equations (SPDE), change of support problem (COSP), soil moisture

1. Introduction

Spatial data fusion is a critical challenge in environmental and ecological statistics, where data are often from different sources (Berrocal et al., 2012), such as point measurements (e.g., sensors) and areal or gridded data (e.g., satellite pixels, administrative units). This paper develops a spatio-temporal Integrated Nested Laplace Approximation

and the Stochastic Partial Differential Equations approach (INLA-SPDE) data fusion framework that combines point data and gridded data, enabling fine resolution predictions. Methodologically, this is related to the change-of-support problem (COSP), which merges datasets observed at different supports, resolutions, and locations, as formalised by Gotway and Young (2002). We also address spatial misalignment, where the response and/or covariates are measured at different locations (Gryparis et al., 2009), which is a practically challenging issue (Scott, 2023).

Fundamental work on spatial data fusion and the change-of-support problem is often referred to as Bayesian melding. Bayesian melding merges point and gridded data through a latent spatial field and introduces aggregation methods to map the latent process to the specific spatial support and accommodate support-specific measurement errors. For example, Gelfand et al. (2001) introduce a unified Bayesian approach for prediction across multiple combinations of point and block supports, applying fully Bayesian kriging and explicitly considering support aggregation and disaggregation in the likelihood. Fuentes and Raftery (2005) develop Bayesian melding for fusing point observations and numerical model outputs, assuming both data types arise from a shared latent Gaussian process with explicit bias correction and uncertainty propagation. Wikle and Berliner (2005) propose hierarchical conditioning to combine information across spatial scales, and Gotway and Young (2007) present a geostatistical framework compatible with GIS implementations that incorporates data supports, handles covariate misalignment, and enables prediction with uncertainty. Spatio-temporal extensions include Sahu et al. (2010). For scalability, Nguyen et al. (2012) introduce SSDF using Fixed Rank Kriging (FRK) within an SRE model to provide low-rank covariance representations. Related developments consider mismatched spatial and temporal scales and flexible latent-field constructions (Wilkie et al., 2019; Wang and Furrer, 2019).

Building upon this foundation, many recent studies obtain advanced computational efficiency and flexibility by using the INLA-SPDE approach that represents the latent field via Gaussian Markov random fields on triangulated meshes (Lindgren et al., 2011). Moraga et al. (2017) introduce a geostatistical model for point-level and area-level spatial data within the INLA-SPDE framework, computing basis-function integrals over grid supports so both point and gridded data inform the latent field. He and Wong (2024) introduce the time dimension to the data fusion model based upon the work of Moraga et al. (2017) that combines in-situ sensor data and satellite data. However, they model the covariate as fixed effects, which doesn't allow for covariate misalignment. Wilson and Wakefield (2020) use SPDE-based continuous spatial models to introduce area-level random effects while incorporating point data. Related work includes methodological improvements and applications in different fields (Suen et al., 2025; Zhong and Moraga, 2023; Cameletti et al., 2019; Forlani et al., 2020; Villejo et al., 2025).

Covariate misalignment, where the response and covariates are observed at different spatial locations (and possibly on different supports), is common in the real world. Spatial regression models (Cressie and Wikle, 2015) often assume the response and covariates are observed at the same locations, which is usually not true in the real world. Many approaches cannot accommodate misaligned covariates and instead require both covariates and response to be measured at the same locations and times, or they treat all data types as point-level, ignoring areal characteristics. Nearest-neighbour alignment underestimates parameter variability. The krige-and-regress (KNR) method (Szpiro et al., 2011) aligns covariates to the response via kriging and uses Monte Carlo or bootstrap correc-

tions for coefficient variance (Madsen et al., 2008; Szpiro et al., 2011; Pouliot, 2023), but typically considers a single misaligned covariate and assumes linear relationships.

Spatio-temporal latent field models further motivate fusion under misalignment. Cameletti et al. (2013) develop a hierarchical spatio-temporal model with a continuously indexed Gaussian field (Matérn covariance) and autoregressive (AR) temporal dynamics, implemented efficiently for prediction and parameter estimation. Earlier spatio-temporal downscaling linked point and gridded processes without misaligned covariates (McMillan et al., 2010). Krainski et al. (2018) show a joint model that allows spatial misalignment between response and covariate, but only in space and not in time.

To the best of our knowledge, many data fusion methods exist, but a key gap remains: misaligned covariates are typically treated as fixed effects or aligned to the response, with no original support for modelling or uncertainty propagation in space and time. We fill this gap with a Bayesian hierarchical framework with an INLA-SPDE approach that (i) models covariates as latent spatio-temporal fields on their own supports, (ii) maps both responses and covariates to observation supports (point or gridded data) via explicit aggregation operators in the likelihood, and (iii) sets different measurement errors for point sensors and gridded satellite data which reflect the fact that the two data sources have different noise characteristics.

Our motivating application is soil moisture mapping in the Elliot Water catchment (Angus, Scotland). We fuse in-situ sensor measurements with gridded satellite products while accounting for covariate misalignment and change of support. The in-situ monitoring network includes 10 rainfall gauges and 22 soil sensors (soil temperature and soil moisture), and the satellite product provides gridded soil moisture estimates. This setting directly inspires our simulation design. The paper is structured as follows. Section 2 describes the spatio-temporal data fusion model developed to address the misaligned covariates and the change-of-support problem, as well as the INLA-SPDE approach used for fitting and inferring the proposed model. Section 3 presents the simulation study used to validate the data fusion model under different scenarios motivated by the real dataset. Section 4 presents the real-world application using soil moisture data from the Elliot Water catchment in Scotland, UK. Section 5 concludes the paper with the key findings of this study, along with the reflections and future work.

2. Methodology

2.1. The framework of Integrated Nested Laplace Approximation (INLA)

INLA focuses on models that can be expressed as latent Gaussian Markov random fields (GMRF). The INLA framework can be described as follows: $\mathbf{y} = (y_1, \dots, y_n)$ is a vector of observed variables whose distribution is in the exponential family, and the mean μ_i (for observation y_i) is linked to the linear predictor η_i using an appropriate link function. The linear predictor can include fixed effects and different random effects. \mathbf{X} denotes the matrix of all latent effects which include the linear predictor, coefficients, and the distribution of the vector of latent effects is assumed to be Gaussian Markov random field (GMRF) with a zero mean and precision matrix $\mathbf{Q}(\theta_2)$, with θ_2 a vector of hyperparameters. The distribution of \mathbf{y} will depend on some vector of hyperparameters θ_1 . The vectors of all hyperparameters in the model will be denoted by $\theta = (\theta_1, \theta_2)$.

Observations are assumed to be independent, given the latent effects and the hyperparameters, which means the likelihood can be written as

$$\pi(\mathbf{y} \mid \mathbf{x}, \boldsymbol{\theta}) = \prod_{i \in \mathcal{I}} \pi(y_i \mid \eta_i, \boldsymbol{\theta}),$$

where set \mathcal{I} contains indices for all observed values of \mathbf{y} .

The joint posterior distribution of the effects and hyperparameters can be expressed as:

$$\pi(\mathbf{x}, \boldsymbol{\theta} \mid \mathbf{y}) \propto \pi(\boldsymbol{\theta}) \pi(\mathbf{x} \mid \boldsymbol{\theta}) \prod_{i \in \mathcal{I}} \pi(y_i \mid x_i, \boldsymbol{\theta})$$
$$\propto \pi(\boldsymbol{\theta}) |\mathbf{Q}(\boldsymbol{\theta})|^{1/2} \exp \left\{ -\frac{1}{2} \mathbf{x}^{\top} \mathbf{Q}(\boldsymbol{\theta}) \mathbf{x} + \sum_{i \in \mathcal{I}} \log \left(\pi(y_i \mid x_i, \boldsymbol{\theta}) \right) \right\},$$

where $\mathbf{Q}(\boldsymbol{\theta})$ to represent the precision matrix of the latent effects.

The marginal distributions for the latent effects and hyperparameters can be calculated from:

$$\boldsymbol{\pi}(x_i \mid \mathbf{y}) = \int \boldsymbol{\pi}(x_i \mid \boldsymbol{\theta}, \mathbf{y}) \, \boldsymbol{\pi}(\boldsymbol{\theta} \mid \mathbf{y}) d\theta,$$

and

$$\pi\left(\theta_{j}\mid\mathbf{y}\right)=\int\pi(oldsymbol{ heta}\mid\mathbf{y})d heta_{-j}.$$

Since both of the marginal distributions include integration over the space of the hyperparameters, and the dimension of $\boldsymbol{\theta}$ depends on the number of observations, which means that numerical integration is difficult for high dimensional data, a good approximation of the joint posterior distribution of the hyperparameters is required. Rue et al. (2009) approximate $\boldsymbol{\pi}(\boldsymbol{\theta} \mid \mathbf{y})$, denoted by $\tilde{\boldsymbol{\pi}}(\boldsymbol{\theta} \mid \mathbf{y})$, which is achieved by using the computational properties of GMRF and the Laplace approximation for multidimensional integration, and use this to approximate the posterior marginal of the latent parameter x_i as:

$$\tilde{\boldsymbol{\pi}}\left(x_{i} \mid \mathbf{y}\right) = \sum_{k} \tilde{\boldsymbol{\pi}}\left(x_{i} \mid \theta_{k}, \mathbf{y}\right) \times \tilde{\boldsymbol{\pi}}\left(\theta_{k} \mid \mathbf{y}\right) \times \Delta_{k},$$

where Δ_k are the weights associated with a vector of values θ_k of the hyperparameters in a grid.

2.2. SPDE approach

Lindgren et al. (2011) consider a stochastic partial differential equation (SPDE) whose solution is a Gaussian field (GF) with Matérn correlation and proposes a new approach to represent a GF with Matérn covariance, as a GMRF, by representing a solution of SPDE using the finite element method. The benefit is that the GMRF representation of the GF, which can be computed explicitly, provides a sparse representation of the spatial effect through a sparse precision matrix, which enables the nice computational properties of the GMRF, which can then be implemented in the INLA approach. To be specific, GMRF is a discrete approximation of a Gaussian field. It is obtained by discretising the continuous domain into a grid or lattice of points. In a GMRF, the values

at each grid point are assumed to be conditionally independent of all other points, given their neighbouring points. This conditional independence property is often represented using a sparse precision matrix (also known as an inverse covariance matrix), where nonzero entries indicate dependencies between neighbouring points. GMRFs provide a computationally efficient way to model and analyse large spatial datasets.

The linear fractional SPDE can be defined as:

$$(\kappa^2 - \Delta)^{\alpha/2} u(\mathbf{x}) = \mathbf{W}(\mathbf{x}), \quad \mathbf{x} \in \mathbb{R}^d, \quad \alpha = \nu + d/2, \quad \kappa > 0, \quad \nu > 0,$$
 (1)

where d denotes the dimension of the spatial domain, $u(\mathbf{x})$ denotes the latent field, Δ is the Laplacian operator: $\Delta = \sum_{i=1}^{d} \frac{\partial^2}{\partial x_i^2}$ and $\mathbf{W}(\mathbf{x})$ denotes a spatial white noise Gaussian stochastic process with unit variance.

Given n observations $y_i, i = 1, ..., n$, at locations \mathbf{x}_i , the following model can be defined:

$$\mathbf{y} \mid \beta_0, \mathbf{u}, \sigma_e^2 \sim N\left(\beta_0 + \mathbf{A}\mathbf{u}, \sigma_e^2\right),$$
 (2)

$$\mathbf{u} \sim GF(0, \Sigma),$$
 (3)

where β_0 is the intercept, **A** is the projection matrix and **u** is a spatial Gaussian random field. Note that the projection matrix **A** links the spatial Gaussian random field (defined using the mesh nodes, which are similar to the integration points on a numeric integration algorithm) to the locations of observed data.

2.3. Gaussian random field process

A Gaussian field (GF) process can be denoted by $u(\mathbf{x})$, where \mathbf{x} is any location in a study area \mathbf{D} . $u(\mathbf{x})$ is a stochastic process, with $\mathbf{x} \in \mathbf{D}$, where $\mathbf{D} \subset \mathbb{R}^d$. For example, \mathbf{D} is a domain and data have been collected at geographical locations, over d=2 dimensions within this domain. The continuously indexed GF is assumed to be continuous over space and implies that it is possible to collect data at any finite set of locations within the domain. To complete the specification of the distribution of $u(\mathbf{x})$, it is necessary to define its mean and covariance. A very simple way to define a correlation function is based only on the Euclidean distance between locations, which assumes that when two pairs of points are equally distant from each other, they will exhibit an equivalent level of correlation. Matérn covariance is another widely used way to define the correlation function, with further details in the next section.

In many scenarios, it is commonly assumed that there exists an underlying GF that cannot be directly observed. Instead, observations are data with a measurement error e_i ,

$$y\left(\mathbf{x}_{i}\right)=u\left(\mathbf{x}_{i}\right)+e_{i},$$

where e_i is independent of e_j for all $i \neq j$ and e_i follows a Gaussian distribution with zero mean and variance σ_e^2 . The covariance of the marginal distribution of $y(\mathbf{x})$ at a finite number of locations is $\Sigma_y = \Sigma + \sigma_e^2 \mathbf{I}$.

2.4. The Matérn covariance

The Matérn covariance is widely used in various scientific fields to define the covariance function Σ , and the reason it is used here is that GF $u(\mathbf{x})$ with the Matérn covariance is a solution to the linear fractional SPDE shown in Equation (1).

For two locations \mathbf{x}_i and \mathbf{x}_j , the stationary and isotropic Matérn correlation function is defined as:

$$\operatorname{Cor}_{M}\left(u\left(\mathbf{x}_{i}\right), u\left(\mathbf{x}_{j}\right)\right) = \frac{1}{2^{\nu-1}\Gamma(\nu)} \left(\kappa \left\|\mathbf{x}_{i} - \mathbf{x}_{j}\right\|\right)^{\nu} K_{\nu} \left(\kappa \left\|\mathbf{x}_{i} - \mathbf{x}_{j}\right\|\right), \tag{4}$$

where $\|.\|$ denotes the Euclidean distance and K_{ν} is the modified Bessel function of the second kind and ν is the order. To be specific, the modified Bessel function of the second kind is the function $K_{\nu}(z)$ with $z = \kappa \|x_i - x_j\|$, which is one of the solutions to the modified Bessel differential equation. κ is a scaling parameter, which can also be interpreted as a range parameter ρ , representing the Euclidean distance at which x_i and x_j become almost independent. The empirically derived definition $\rho = \sqrt{0.8\nu/\kappa}$, corresponds to correlation near 0.1 at the distance ρ , for all ν .

The Matérn covariance function is $\sigma_u^2 \operatorname{Cor}_M(u(\mathbf{x}_i), u(\mathbf{x}_j))$, where σ_u^2 is the marginal variance of the process and is defined as:

$$\sigma_u^2 = \frac{\Gamma(\nu)}{\Gamma(\nu + d/2)(4\pi)^{d/2}\kappa^{2\nu}}.$$

2.5. Spatio-only data fusion model framework

Next, we will construct our fusion model. First, we will define a

spatio-only data fusion model built upon a geostatistical framework, before extending this framework to the full spatial temporal framework. The model assumes that there is a spatially continuous variable underlying all observations that can be modelled using a Gaussian random field process (Moraga et al., 2017; Zheng et al., 2024). Let D denote the set of points with real number coordinates in a two-dimensional plane. The process is denoted by $\mu = \{\mu(\mathbf{s}) : \mathbf{s} \in D \subset \mathbb{R}^2\}$, has mean function $\mathbb{E}[\mu(\mathbf{s})] = 0$ and stationary covariance function $\mathrm{Cov}(\mu(\mathbf{s}), \mu(\mathbf{s}')) = \Sigma(\mathbf{s} - \mathbf{s}')$. Conditionally on $\mu(\mathbf{s})$, point data Y_i observed at a finite set of sites, say $\mathbf{s}_i \in D, i = (1, \dots, I)$, are mutually independent with

$$Y(\mathbf{s}_i) \mid \mu(\mathbf{s}_i) \sim N(x(\mathbf{s}_i) + \mu(\mathbf{s}_i), \tau^2),$$

where $x(\mathbf{s}_i)$ represents the large-scale structure of the spatial process, capturing broad variation across the study catchment. Rather than assuming a constant mean, $x(\mathbf{s}_i)$ allows the expected value of the response variable to vary with location \mathbf{s}_i , reflecting the influence of spatially distributed covariates such as elevation and soil type. It can be interpreted as a smoothly varying surface that describes the average behaviour of the response variable across space using a mean function, while the remaining spatial random field $\mu(\mathbf{s}_i)$ accounts for variation not explained by the mean function. The τ represents the standard deviation, measuring how much the observations are spread out around the mean

The geostatistical model framework can be defined as follows for point data and grid data, respectively. Point data observations in location $\mathbf{s}_i, i = (1, 2, ..., I)$. Gridded data observations are defined as block averages in blocks $\mathbf{B}_j \subset D, j = (1, 2, ..., J)$, while a

block \mathbf{B}_j is a measurable subset of D with $|\mathbf{B}_j| > 0$, over which spatial processes $x(\mathbf{s})$ and $\mu(\mathbf{s})$ are averaged (Moraga et al., 2017).

$$Y_k(\mathbf{s}_i) = \alpha + x(\mathbf{s}_i) + \mu_k(\mathbf{s}_i) + e_k^{(p)}(\mathbf{s}_i), \quad i = 1, \dots, I$$

$$(5)$$

$$Y_k(\mathbf{B}_j) = |\mathbf{B}_j|^{-1} \int_{\mathbf{B}_j} (\alpha_k + x(\mathbf{s}) + \mu_k(\mathbf{s})) d\mathbf{s} + e_k^{(g)}(\mathbf{B}_j), \quad |\mathbf{B}_j| > 0,$$
 (6)

where k = 1, 2, ..., K denote the index for K different variables (such as environmental factors) and B_j denotes a block in domain D and $|\mathbf{B}_j| = \int_{\mathbf{B}_j} 1d\mathbf{s}$ denotes the area of \mathbf{B}_j , and $e_k^{(p)}(\mathbf{s}) \sim N(0, \tau_k^{(p)^2})$ and $e_k^{(g)}(\mathbf{B}) \sim N(0, \tau_k^{(g)^2})$ are uncorrelated error terms defined by Gaussian white-noise processes. Note, that the variance parameters are not shared between the point and grid/areal error terms as the errors can be structural different between the two different modalities

The projection matrix A specified in the SPDE approach is designed to deal with point data, and many past studies treat gridded data as point data by using the centroid locations of the grid, thereby overlooking the inherent characteristics of gridded data. A novel way to construct the projection matrix A is proposed by Moraga et al. (2017), which specifies that a particular observation in area **B** and the process μ is linked through the mean value of the random field in the entire area: $\mu(\mathbf{B}) = |\mathbf{B}|^{-1} \int_{B_i} \mu(\mathbf{s}) d\mathbf{s}$, where $|\mathbf{B}|$ denotes the area of B. The integral defines the theoretical relationship between the latent field $\mu(\mathbf{s})$ and the gridded observation $Y_k(\mathbf{B}_i)$, and represents the true unobserved block average over the entire area B_i . However, computing the integral of $\mu(s)$ is challenging because it is a continuous process, but the mesh vertices used here only have discrete points. In the projection matrix, each row of A corresponds to a particular observation in block \mathbf{B}_{i} . The elements in each row are weights assigned to mesh vertices inside \mathbf{B}_{i} , which are usually 1/H, where H is the number of vertices of the mesh in \mathbf{B}_j . So this approximates the integral as $\mu(B_j) \approx \frac{1}{H} \sum_{h=1}^{H} \mu(s_h)$, where s_h are vertices in \mathbf{B}_j . Thus, A acts as a numerical integration operator, converting the continuous integral into a tractable discrete average. The integral of the process in each grid is approximated by taking the average of the vertex weights in the corresponding cell.

2.6. Spatio-temporal data fusion model framework

Building from the spatial formulation, this section introduces a spatio-temporal data fusion framework that combines point and gridded data under change of support, explicitly handles misaligned covariates and responses, and allows different measurement errors. He and Wong (2024) extend a spatial-only data fusion model to a spatio-temporal data fusion model, building upon the work from Moraga et al. (2017). However, their model framework treats covariates only as fixed effects, so misaligned covariates cannot be accommodated in the framework. We address this issue with a flexible framework which leverages multiple covariates with possibly independent spatial support by modelling selected covariates as individual latent spatio-temporal fields and mapping both responses and covariates to observation supports via aggregation operators. This explicitly handles misaligned covariates and responses, and also allows different measurement errors for point sensors and gridded data. In our model, the response is driven by its

own latent field together with the latent fields of the covariates. Our spatio-temporal data fusion model framework is built based Equation (5) and (6) and defined as follows:

Let $D \subset \mathbb{R}^2$ denote the spatial dimension and $T \subset \mathbb{R}$ the temporal dimension. The point observations are denoted as Y(s,t). The $\mu(s)$ denotes the spatio-only process, which is a Gaussian distribution with a Matérn covariance structure that is independent of time. The latent spatio-temporal process is defined as $\eta = \{\eta(s,t) : s \in D, t \in T\}$, with mean function $\mathbb{E}[\eta(s,t)] = 0$. We model temporal dependence in the latent field using an autoregressive process which for this paper we assume is of order 1 (AR(1)) based on the characteristics of the data (Cressie and Wikle, 2015).

$$\eta(\mathbf{s}, t) = a * \eta(\mathbf{s}, t - 1) + \sqrt{1 - a^2} * \mu(\mathbf{s}, t), \quad t = 2, \dots, T,$$
(7)

where a denotes the temporal autoregressive coefficient satisfying |a| < 1 to ensure stationarity, $\mu(s,t) \sim \mathrm{GP}(0,\Sigma(s,s'))$ is a spatially correlated innovation term which has a Gaussian distribution with a Matérn covariance structure that is independent of time, and initial stage when t=0: $\eta(s,t) \sim N\left(0,\frac{\tau^2}{1-a^2}\right)$. To be specific, the covariance function with a Matérn covariance structure is as follows:

$$\operatorname{Cov}_{M}(\mu(\mathbf{s}, t'), \mu(\mathbf{s}', t')) = \frac{1}{2^{\nu - 1}\Gamma(\nu)} (\kappa \|\mathbf{s} - \mathbf{s}'\|)^{\nu} K_{\nu} (\kappa \|\mathbf{s} - \mathbf{s}'\|),$$
(8)

where $\|.\|$ denotes the Euclidean distance and K_{ν} is the modified Bessel function of the second kind and ν is the order, with the parameter and function interpretations the same/similar as in Equation (4).

The Matérn covariance function $\operatorname{Cov}_M(\mu(\mathbf{s},t'),(\mu(\mathbf{s}',t')))$ defines the dependency structure between two location values measured at the same time point. It is noted that the dependency structure does not account for temporal dependence. Specifically, the covariance between two observations at the same time point is given by

$$Cov_M(\mu(s, t'), \mu(s', t')) = \Sigma(s - s'),$$

while the covariance between observations at different time points is assumed to be zero:

$$\operatorname{Cov}_M(\mu(s,t),\mu(s',t')) = 0$$
 for $t \neq t'$.

This implies that the spatio-only latent field $\mu(s,t)$ is correlated only in the spatial dimension and independent over time. The Cov_M denotes the spatial Matérn covariance, but it is noted that we model a day-specific spatial field that is independent across days, while the temporal dependence is handled by a separate term AR(1). Each variable can be assigned its own independent latent process $\eta(s,t)$ following this structure.

2.7. Full spatio-temporal data fusion model

The motivation of this study is to make predictions of a variable of interest in both space and time with a set of covariates that are observed both at point locations and as areal observations, which are potentially spatially misaligned from the variable of interest

To formalise this, suppose we have a collection of K different variables (i.e. y_k) which can be observed at either point locations or at an areal (grid) level. For the kth variable,

define the point locations where it is measured as $\mathbf{s}^{(k)}$ and the areal regions where it is measured as $\mathbf{B}^{(k)}$.

Further, suppose there is an additional variable (namely the variable of interest) which we wish to predict at unknown locations which for notational convenience we will refer to as y_{K+1} with corresponding point observation points as $\mathbf{s}^{(K+1)}$ and the areal observation regions as $\mathbf{B}^{(K+1)}$. Note that due to sensor placement, it is highly likely that for some i and j with $i \neq j$ that $\mathbf{s}^{(i)} \cap \mathbf{s}^{(j)} \neq \emptyset$. The reverse is also true, with it being very likely (as we will see in the real data application) that there exist pairs of i and j such that $\mathbf{s}^{(i)} \cap \mathbf{s}^{(j)} = \emptyset$. Moreover, and crucially for the task at hand, it is possible that $\mathbf{s}^{(i)} \cap \mathbf{s}^{(K+1)} = \emptyset$, i.e. that there are covariates that are misaligned from the quantity of interest, which motivates this study.

Our framework is as follows where with a slight abuse of notation we represent $y_k\left(\mathbf{s}_j^{(k)},t\right)$ as the observation of the k-th variable at it's j-th point location at time t, $y_k\left(\mathbf{B}_j^{(\mathbf{k})},t\right)$ as the areal observation of the variable k at the j-th areal observation point at time t. Thus, for $k \in \{1,\ldots,K\}$, $j_1 \in \{1,\ldots,|\mathbf{s}^{(k)}|\}$ and $j_2 \in \{1,\ldots,|\mathbf{B}^{(k)}|\}$:

$$y_k\left(\mathbf{s}_{j_1}^{(k)}, t\right) = \alpha_k + \eta_k\left(\mathbf{s}_{j_1}^{(k)}, t\right) + e_k^{(p)}\left(\mathbf{s}_{j_1}^{(k)}, t\right)$$

$$y_k\left(\mathbf{B}_{\mathbf{j_2}}^{(\mathbf{k})}, t\right) = \frac{1}{\left|\mathbf{B}_{\mathbf{j_2}}^{(\mathbf{k})}\right|} \int_{\mathbf{B}_{j_2}^{(\mathbf{k})}} \left[\alpha_k + \eta_k(\mathbf{s}, t)\right] d\mathbf{s} + e_3^{(g)}\left(\mathbf{B}_{\mathbf{j_2}}^{(\mathbf{k})}, t_m\right). \tag{9}$$

where $\eta_k(s,t)$ is defined as in Equation 7 and thus has an additional AR(1) parameter for each k which we denote as a_k . Thus, allowing us to have a fully spatial-temporal prediction of the K covariates in question, regardless of their misalignment. Additionally we wish to consider the set of variables which we can measure at all locations, e.g. in an environmental setting elevation. Let us assume that there are l such variables and that $x(s,t) \in \mathbb{R}^l$ is a vector of such variables at location s and time t. This then allows the construction of the most generic functional form for the prediction of our variable of interest:

$$y_{K+1}\left(\mathbf{s}_{j}^{(K+1)},t\right) = \alpha_{K+1} + f\left(x\left(\mathbf{s}_{j}^{(K+1)},t\right),\eta_{1}\left(\mathbf{s}_{j}^{(K+1)},t\right),\dots,\eta_{K}\left(\mathbf{s}_{j}^{(K+1)},t\right)\right) + \eta_{K+1}\left(\mathbf{s}_{j}^{(K+1)},t\right) + e_{K+1}^{(p)}\left(\mathbf{s}_{j}^{(K+1)},t\right),$$
(10)

$$y_{K+1}\left(\mathbf{B}_{j}^{(K+1)},t\right) = \frac{1}{\left|\mathbf{B}_{j}^{(K+1)}\right|} \int_{\mathbf{B}_{j}^{(K+1)}} \left[\alpha_{K+1} + f(x(s,t),\eta_{1}(s,t),\dots,\eta_{K}(s,t)) + \eta_{K+1}(s,t)\right] d\mathbf{s} + e_{K+1}^{(g)}\left(\mathbf{B}_{j}^{(K+1)},t_{m}\right),$$

$$(11)$$

where f is a generic function representing the impact of each of the covariates on the quantity of interest. In practice, we assume that f is linear, giving the following form that can be estimated using the INLA-SPDE framework:

$$y_{K+1}\left(\mathbf{s}_{j}^{(K+1)}, t\right) = \alpha_{K+1} + \theta^{T} x \left(\mathbf{s}_{j}^{(K+1)}, t\right) + \sum_{k=1}^{K} \beta_{k} \, \eta_{k} \left(\mathbf{s}_{j}^{(K+1)}, t\right) + \eta_{K+1} \left(\mathbf{s}_{j}^{(K+1)}, t\right) + e_{K+1}^{(p)} \left(\mathbf{s}_{j}^{(K+1)}, t\right).$$

$$(12)$$

$$y_{K+1}\left(\mathbf{B}_{j}^{(K+1)},t\right) = \frac{1}{\left|\mathbf{B}_{j}^{(K+1)}\right|} \int_{\mathbf{B}_{j}^{(K+1)}} \left[\alpha_{K+1} + \theta^{T} x(s,t) + \sum_{k=1}^{K} \beta_{k} \, \eta_{k}(s,t) + \eta_{K+1}(s,t)\right] \, \mathrm{d}\mathbf{s} + e_{K+1}^{(g)}\left(\mathbf{B}_{j}^{(K+1)},t_{m}\right).$$

$$(13)$$

where $\theta^T \in \mathbb{R}^l$ is the coefficients for the linear terms corresponding to the variables observed at all locations, $\beta_1, \ldots \beta_K$ are the terms for the variables with a mixture of point and areal observations, α_{K+1} is the constant term for the variable of interest, finally, $e_{K+1}^{(p)}\left(\mathbf{s}_j^{(K+1)},t\right)$ and $e_{K+1}^{(g)}\left(\mathbf{B}_j^{(K+1)},t_m\right)$ are the error terms for the point and areal measures respectively.

In practice, the INLA-SPDE fitting step combines both point and gridded data to produce posterior means of each latent field at the mesh nodes, which are used to compute predictions at unknown locations (Moraga et al., 2017). The predicted value $\hat{y}_{K+1}(s,t)$ in any unknown locations s at time t within domain D is given by,

$$\hat{y}_{K+1}(s,t) = \hat{\alpha}_{K+1} + \hat{\theta}^T x(s,t) + \sum_{k=1}^K \hat{\beta}_k \, \hat{\eta}_k(s,t) + \hat{\eta}_{K+1}(s,t). \tag{14}$$

Equation (14) uses parameters estimated in the INLA-SPDE approach to construct predictions for the response variable Y_{K+1} . Each element of the prediction model is estimated as follows. The intercept term $\hat{\alpha}_{K+1}$ is obtained as the posterior mean of the corresponding fixed effect in the INLA model. The regression coefficients $\hat{\theta}$ of the covariate $x(\mathbf{s},t)$ is also estimated as a fixed effect using posterior marginals from the INLA-SPDE approach. The scaling parameters $\hat{\beta}_k$, which are the weights of the contributions of the latent spatial fields $\hat{\eta}_k(\mathbf{s},t)$, are similarly estimated as fixed effects within the hierarchical model.

The latent fields $\hat{\eta}_k(\mathbf{s},t)$, are modelled using the INLA-SPDE approach, which approximates the continuous spatial fields with Gaussian Markov random fields (GMRFs) defined using triangulated meshes. Their posterior means at the mesh nodes are computed during the model fitting step and then projected to the prediction locations through the basis functions of the SPDE mesh (Lindgren and Rue, 2015). The spatial smoothness, range, and marginal variance of each latent field are treated as hyperparameters, inferred from their posterior distributions, and summarised by posterior means.

The predicted response $\hat{Y}_{K+1}(\mathbf{s},t)$ is constructed by combining the estimated intercept, the scaled covariate effect, the weighted contributions from the two latent fields, and the direct latent field representing Y_{K+1} . Although predictions can be generated for all variables, the focus here is on evaluating predictive performance specifically for the response variable Y_{K+1} . In generating predictions, the outputs from the fine-resolution maps are treated as point data.

Note that this functional form can be seen as an extension to that in He and Wong (2024). In their model, covariates enter only as fixed effects, whereas our general framework allows covariates to be included either as fixed effects (with appropriate coverage) or as latent spatio-temporal fields with areal and/or point observations.

3. Simulation study

This simulation study evaluates the predictive performance of a spatio-temporal datafusion model that integrates sparse point measurements with gridded data, examining how the number of time points (t) and covariate missingness affect prediction and parameter estimation. We deal with the change-of-support problem for point and gridded data following Moraga et al. (2017), add misaligned covariates, and extend the model to the spatio-temporal setting to borrow information across space and time. We also identify the minimum number of time points needed for reliable predictions (as measured by RMSE), providing practical guidance for deployments with sparse sensor networks. To assess the predictive performance of the spatio-temporal data fusion model, we conduct three simulation studies: (i) a spatial-prediction study that predicts values at unobserved locations on the final day of training; (ii) a spatio-temporal prediction study that predicts at unobserved locations one day ahead (outside the training period), testing temporal interpolation and spatial generalisation; and (iii) a robustness study that evaluates performance under realistic patterns of missingness in the gridded covariates. Together, these analyses provide a comprehensive assessment of the model's ability to fuse sparse point sensor data with satellite gridded data while maintaining accuracy across different settings.

In the simulation design, we consider three variables: y_1 , y_2 , and y_3 . The variable y_3 represents the response, while y_1 and y_2 represent covariates (and thus K=2). Among the covariates, y_1 is spatially misaligned with the response, observed at 10 independent point locations (i.e. $\mathbf{s}^{(1)} \cap \mathbf{s}^{(3)} = \emptyset$), whereas y_2 is aligned and observed at the same 22 point locations as y_3 (i.e. $\mathbf{s}^{(2)} = \mathbf{s}^{(3)}$). To mimic real data settings, each variable can be generated and observed as either point data or gridded data. The generation of spatio-temporal data in the simulation study follows the methodology in Section 2. We generate latent spatial fields as Matérn GRFs using 100 independent seeds. For each seed, we build datasets with $t \in \{3,7,10\}$ time points using the same underlying realisations, so differences come from the number of time points t rather than spatial randomness. We then introduce temporal correlation by specifying an separate AR(1) process for each variable. We generate point and gridded observations by adding independent Gaussian measurement noise to the latent fields, with different variances to reflect their measurement errors. For gridded data, we average 10,000 field estimations within each cell to approximate gridded means. We then include a large-scale trend covariate x(s,t) = 0.2 Easting + 0.3 Northing with $\theta_1 = -0.2$. For each simulation, we uniformly sample 22 locations without replacement and set up two test scenarios for y₃: 20 held-out locations on the final training day and the same 20 locations one day ahead. The true parameter values $(\alpha, \beta, \theta, \rho, \sigma^2, a)$ are given in Table A.5 and are chosen based on both previous studies and real data characteristics to make sure that they are both theoretically reliable and practically feasible. See Appendix A for full implementation details including Figure A.4 which illustrates the workflow.

Overall, the simulation study gives a substantial workload and a comprehensive assessment of fusion performance for point and gridded data under different spatial and temporal conditions.

3.1. Final-day predictions at unobserved locations on the last day of the training period with varying time points.

We compare the prediction performance and parameter estimation of the point-only, grid-only, and joint (fusion) models for final-day predictions at unobserved locations, varying the number of time points t. Table 1 and 2 presents the parameter estimation performance with the RMSE and mean of the spatio-temporal point, grid, and joint models across varying numbers of time points (t) on simulation datasets. Most parameter RMSE values decrease with increasing t, suggesting improved estimation accuracy. Notably, the joint model consistently outperforms both the point and grid models, with lower RMSE values in most scenarios. This performance shows the joint model's ability to outperform the other two models in the spatio-temporal scenario, effectively borrowing information across both dimensions. In contrast, the point and grid models exhibit less accurate estimated parameters, which suggests that fusing different data sources improves the parameter estimation.

The RMSE improvement is very obvious as t increases from 3 to 7 time points, suggesting that temporal information enhances estimation by reducing uncertainty through repeated measurements on the same locations. However, beyond t=7, the improvement stabilises, with little difference observed between t=7 and t=10. This plateau implies a threshold where additional temporal data adds limited information for parameter estimation, perhaps because the model has already captured much of the temporal structure. From a real data application perspective, this finding suggests that allocating resources to increase temporal resolution beyond t=10 may not guarantee better prediction performance. Instead, refining spatial resolution or incorporating more data sources could be more helpful for further model improvements.

The first step to validate the spatio-temporal data fusion model is to assess its predictive performance at the time boundary of the training period. In this simulation study, the whole dataset spans 100 days, with the final day used as the test set. From this day, 20 unobserved locations are randomly selected as test points. The training set consists of the last t days, including the final day, and is used to train the model. Predictions are made for the test points on the last day. We predict the final-day test points. INLA-SPDE models spatial structure via an SPDE (a GMRF approximation to a Matérn field) and temporal dependence via an AR(1) process. Predictions are calculated using the posterior mean of the latent field, and performance is measured by root mean squared prediction error (RMSPE).

Figure 1 compares predictive accuracy for the point, grid, and joint models at unobserved locations on the final day of the training period. The violin plots show prediction errors (RMSPE $_y$) across 100 simulations, with lower values indicating better performance. As the number of time points increases, the joint model consistently gets the lowest RMSPE $_y$, while the point model shows very little improvement. The spread of the joint model's violin plot also decreases, indicating less across-replicate spread in the simulations. These all together demonstrate that the joint model is more effective at using temporal information to reduce uncertainty when compared to the point and grid models.

Table 1: Posterior summaries of intercept, scaling and variance parameters for the spatio-temporal fusion model (Equation (12) and (13)) in the simulation study when varying both the number of available time points ($t \in \{3, 7, 10\}$) and dataset availability (only point (sensor) dataset/only the grid (areal) data/joint (both) datasets). Posteriors are summarised using the average: posterior mean, 2.5% posterior quantile ($Q_{2.5\%}$) 97.5% posterior quantile, ($Q_{97.5\%}$), and posterior RMSE over the 100 replicates in the study.

(a) Intercept parameters (α)

Param	True		t	= 3			$t = 7 \qquad \qquad t = 10$						
		Mean	$Q_{2.5\%}$	$Q_{97.5\%}$	RMSE	Mean	$Q_{2.5\%}$	$Q_{97.5\%}$	RMSE	Mean	$Q_{2.5\%}$	$Q_{97.5\%}$	RMSE
α_1 point	0.50	0.48	-0.40	1.34	0.42	0.45	-0.14	0.99	0.29	0.47	0.00	0.94	0.24
α_1 grid	0.50	0.48	-0.28	1.19	0.31	0.47	-0.07	0.94	0.21	0.49	0.04	0.88	0.18
α_1 joint	0.50	0.48	-0.28	1.19	0.31	0.47	-0.10	0.97	0.21	0.49	0.01	0.90	0.19
α_2 point	0.80	0.84	0.49	1.10	0.18	0.79	0.57	1.01	0.10	0.79	0.61	1.00	0.08
α_2 grid	0.80	0.84	0.48	1.05	0.15	0.78	0.56	0.99	0.10	0.80	0.60	0.98	0.08
α_2 joint	0.80	0.84	0.52	1.02	0.15	0.79	0.55	0.98	0.09	0.80	0.57	1.02	0.07
α_3 point	1.00	1.34	0.89	2.06	0.42	1.45	1.06	1.96	0.49	1.44	1.17	1.90	0.47
α_3 grid	1.00	1.36	0.47	1.52	0.40	1.43	0.66	1.53	0.46	1.43	0.79	1.52	0.45
α_3 joint	1.00	1.38	0.69	1.62	0.43	1.45	0.91	1.68	0.47	1.44	1.00	1.65	0.46

(b) Scaling parameters ($\beta \& \theta$)

Param	True	t			t	= 7		t = 10				
		Mean $Q_{2.5\%}$						RMSE	Mean	$Q_{2.5\%}$	$Q_{97.5\%}$	RMSE
β_1 grid	-0.30	$ \begin{vmatrix} -0.21 & -0.47 \\ -0.28 & -0.38 \\ -0.28 & -0.34 \end{vmatrix} $	-0.12 (0.08	-0.18	-0.37	-0.21	0.03	-0.15	-0.37	-0.23	0.02
β_2 grid	-0.40	$ \begin{vmatrix} -0.31 & -0.54 \\ -0.33 & -0.55 \\ -0.36 & -0.73 \end{vmatrix} $	-0.01 (0.14 -	-0.40	-0.56	-0.18	0.10	-0.33	-0.56	-0.24	
	-0.20	$ \begin{vmatrix} -0.19 & -0.57 \\ -0.19 & -0.25 \\ -0.18 & -0.25 \end{vmatrix} $	0.26	0.09 -	-0.39	-0.20			-0.33		0.18	0.07 0.08 0.06

(c) Variance parameters (σ^2)

Param	True		t	= 3			t	= 7			t	= 10	
		Mean	$Q_{2.5\%}$	$Q_{97.5\%}$	RMSE	Mean	$Q_{2.5\%}$	$Q_{97.5\%}$	RMSE	Mean	$Q_{2.5\%}$	$Q_{97.5\%}$	RMSE
σ_1^2 point	1.00	1.00	0.72	1.56	0.16	1.04	0.81	1.32	0.10	1.06	0.86	1.29	0.10
σ_1^2 grid	1.00	0.96	0.72	1.25	0.15	0.93	0.78	1.11	0.13	0.91	0.78	1.05	0.14
σ_1^2 joint	1.00	0.92	0.69	1.21	0.17	0.90	0.74	1.09	0.16	0.87	0.74	1.03	0.16
σ_2^2 point	0.50	0.46	0.33	0.64	0.10	0.48	0.39	0.58	0.06	0.49	0.41	0.58	0.05
σ_2^2 grid	0.50	0.45	0.32	0.61	0.07	0.45	0.36	0.55	0.07	0.44	0.37	0.53	0.06
σ_2^2 joint	0.50	0.35	0.24	0.51	0.19	0.39	0.31	0.49	0.15	0.41	0.33	0.51	0.15
σ_3^2 point	0.30	0.32	0.16	0.61	0.07	0.32	0.21	0.46	0.07	0.30	0.22	0.41	0.04
σ_3^2 grid	0.30	0.33	0.21	0.50	0.07	0.30	0.21	0.55	0.03	0.29	0.22	0.38	0.04
σ_3^2 joint	0.30	0.25	0.14	0.42	0.09	0.29	0.20	0.41	0.12	0.28	0.20	0.39	0.10

Table 2: Posterior summaries of range parameters and temporal coefficients for the spatio-temporal fusion model (Equation (12) and (13)) in the simulation study when varying both the number of available time points ($t \in \{3,7,10\}$) and dataset availability (only point (sensor) dataset/only the grid (areal) data/joint (both) datasets). Posteriors are summarised using the average: posterior mean, 2.5% posterior quantile ($Q_{2.5\%}$) 97.5% posterior quantile, ($Q_{97.5\%}$), and posterior RMSE over the 100 replicates in the study.

(a) Range parameters (ρ)

Param	True		t	= 3			t	= 7			t	= 10)				
		Mean	$Q_{2.5\%}$	$Q_{97.5\%}$	RMSE	Mean	$Q_{2.5\%}$	$Q_{97.5\%}$	RMSE	Mean	$Q_{2.5\%}$	$Q_{97.5\%}$	RMSE				
ρ_1 point	4.00	4.91	2.25	9.59	1.74	4.31	2.76	6.43	1.14	4.06	2.82	5.65	0.81				
ρ_1 grid	4.00	4.87	3.04	7.45	1.10	4.78	3.54	6.34	0.94	4.78	3.70	6.09	0.90				
ρ_1 joint	4.00	5.03	3.14	7.73	1.26	5.11	3.76	6.84	1.22	5.08	3.92	6.52	1.17				
ρ_2 point	3.00	3.84	1.75	7.71	1.74	3.12	2.05	4.55	0.39	3.06	2.14	4.22	0.30				
ρ_2 grid	3.00	3.70	1.91	6.64	1.24	3.81	2.55	5.55	0.88	3.82	2.73	5.23	0.90				
ρ_2 joint	3.00	4.57	2.14	8.93	2.52	3.83	2.45	5.76	1.42	3.89	2.69	5.47	1.20				
ρ_3 point	2.00	3.31	1.14	17.85	1.73	3.00	1.63	6.27	1.48	2.60	1.59	4.56	0.87				
ρ_3 grid	2.00	3.39	2.16	11.30	1.65	3.12	2.68	8.60	1.31	2.95	2.55	6.93	1.06				
ρ_3 joint	2.00	2.82	1.27	18.79	1.05	2.62	2.04	8.19	0.80	2.58	1.88	6.18	0.74				

(b) Temporal coefficients (a)

Param	True		t	=3			t	= 7		t = 10				
	Value	Mean	$Q_{2.5\%}$	$Q_{97.5\%}$	RMSE	Mean	$Q_{2.5\%}$	$Q_{97.5\%}$	RMSE	Mean	$Q_{2.5\%}$	$Q_{97.5\%}$	RMSE	
a_1 point	0.40	0.34	-0.15	0.73	0.27	0.33	0.05	0.58	0.20	0.34	0.10	0.56	0.17	
a_1 grid	0.40	0.43	0.12	0.68	0.15	0.39	0.21	0.56	0.06	0.39	0.24	0.53	0.05	
a_1 joint	0.40	0.45	0.13	0.70	0.14	0.44	0.24	0.61	0.08	0.44	0.27	0.58	0.05	
a_2 point	0.50	0.40	-0.03	0.72	0.19	0.45	0.24	0.62	0.13	0.46	0.29	0.61	0.11	
a_2 grid	0.50	0.42	0.04	0.71	0.26	0.44	0.20	0.65	0.11	0.46	0.26	0.63	0.07	
a_2 joint	0.50	0.47	0.04	0.82	0.37	0.60	0.40	0.77	0.20	0.64	0.48	0.78	0.20	
a_3 point	0.60	0.49	-0.16	0.89	0.31	0.59	0.17	0.81	0.15	0.59	0.26	0.81	0.16	
a_3 grid	0.60	0.44	0.10	0.89	0.40	0.57	0.53	0.92	0.15	0.59	0.57	0.90	0.14	
a_3 joint	0.60	0.59	0.14	0.97	0.21	0.61	0.56	0.96	0.10	0.62	0.73	0.95	0.07	

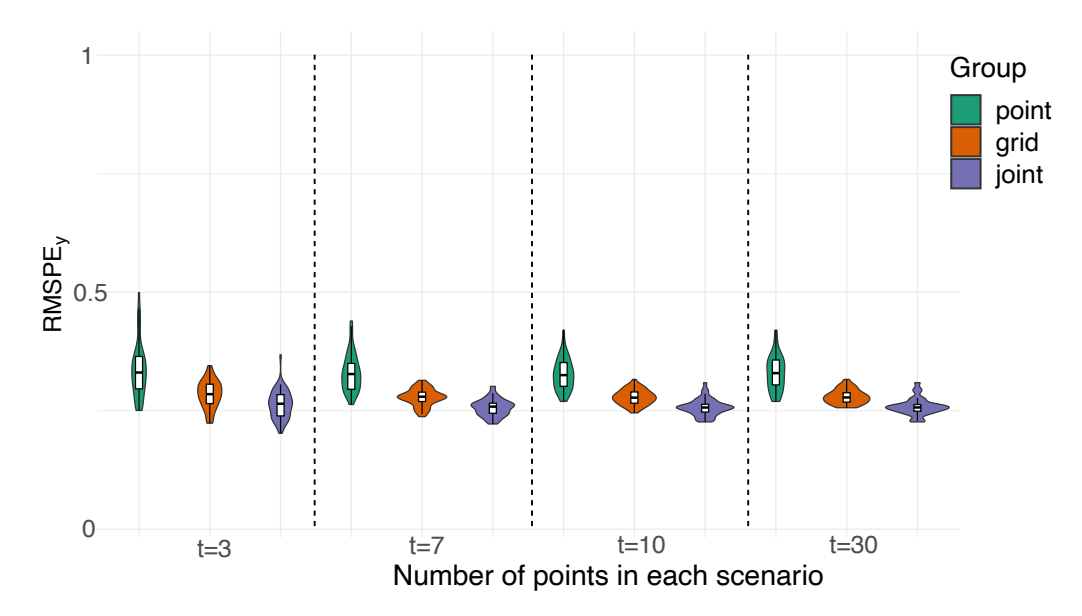


Figure 1: Comparison of prediction error (RMSPE_y) at unobserved locations of point, grid, and joint models with varying numbers of time points $(t \in \{3,7,10,30\})$. Results based on 100 simulations with latent field $(\sigma_1 = 1, \sigma_2 = 0.5, \sigma_3 = 0.3)$ of final day predictions of the last day of the training period.

3.2. One-day-ahead future predictions at unobserved locations beyond the training period with varying time points (t = 3, 7, 10, 30).

In this simulation study, the dataset includes 100 days, with the final day used as the test set. On this day, 20 unobserved locations are randomly selected as test points. The training set consists of the t days immediately before the final day (it excludes the last day) and is used to fit the model. Predictions are then made for the test points on the final day.

Figure 2 shows the one-day-ahead prediction errors (RMSPE $_y$) at unobserved locations. The joint model still outperforms or performs equally well as the point and grid model, though with smaller margins than in Figure 1. All models show higher overall error (0.4-0.6 range) for future predictions beyond the training period, with performance differences remaining relatively stable despite increasing time points. The distributions of the RMSPE $_y$ appear wider, suggesting more variability in one-day-ahead prediction accuracy. This suggests that while temporal information improves model performance, predicting future time points at unobserved locations remains more challenging.

3.2.1. Assessing the model performance under realistic grid covariate missingness

In our real data application case, the only available satellite data is the response variable Soil Water Index (SWI), while all the covariates (e.g., rainfall and temperature) from satellite data are not available. To ensure the proposed model framework remains robust under this setting, a targeted simulation study was designed to mimic the real data scenario. Specifically, we compare the performance of the joint model in two situations: one where gridded data for covariates $(y_1 \text{ and } y_2)$ are available, and another where

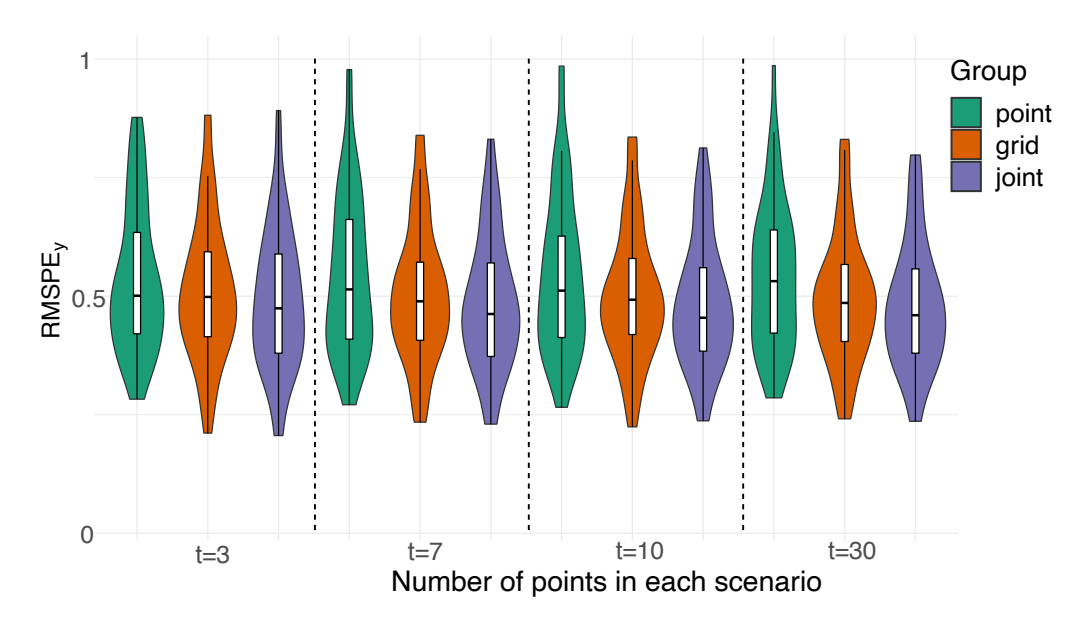


Figure 2: Comparison of prediction error (RMSPE_y) at unobserved locations of point, grid, and joint models with varying numbers of time points $(t \in \{3,7,10,30\})$. Results based on 100 simulations with latent field $(\sigma_1 = 1, \sigma_2 = 0.5, \sigma_3 = 0.3)$ of one-day-ahead predictions of the training period.

gridded data for these variables are completely missing. The point data, including both responses and covariates, are kept identical across both situations.

To reflect the structure of the real application, we fix the number of time points at t=3. The only difference between the two scenarios is the availability of the grid covariates. Table 3 presents the posterior summaries of the joint model parameters under two scenarios: with and without the gridded covariates. Each parameter estimate is summarised using the average: posterior mean, 2.5% posterior quantile ($Q_{2.5\%}$) 97.5% posterior quantile, ($Q_{97.5\%}$), and posterior root mean squared error (RMSE) over the 100 replicates in the study.

The results show that the joint model produces reasonably accurate estimates for the intercept parameters α_1 , α_2 , and α_3 under both scenarios. However, under the gridded covariates missing condition, posterior uncertainty increases slightly, and RMSEs are higher, particularly for α_3 , which appears more sensitive to missing gridded covariates. In contrast, the scaling parameters β_1 , β_2 , and θ_1 are more affected by missing gridded covariates. These parameters show greater posterior variability and higher RMSEs in the grid missing situation, indicating reduced identifiability when covariate information is incomplete. The spatial variance parameters σ_1^2 , σ_2^2 , and σ_3^2 are estimated reasonably well in both scenarios. Although credible intervals are slightly wider and RMSEs slightly higher under the grid missing situation, the estimates remain close to the true values, suggesting the model maintains robustness for these latent fields' variance terms.

However, the spatial range parameters ρ_1 , ρ_2 , and ρ_3 are poorly recovered when the gridded covariates are missing, with posterior means overestimating the true values and large RMSEs. This suggests that the range parameters are structurally difficult to

Table 3: Posterior summaries of parameters for the spatio-temporal fusion joint model (Equation (12) and (13)) in the simulation study varying the availability/missingness of gridded covariates. Experiments are conducted with t=3. Posteriors are summarised using the average: posterior mean, 2.5% posterior quantile ($Q_{2.5\%}$) 97.5% posterior quantile, ($Q_{97.5\%}$), and posterior RMSE over the 100 replicates in the study.

		Grio	ded cova	ariates mi	ssing	Gridded covariates complete					
Param	True	Mean	$Q_{2.5\%}$	$Q_{97.5\%}$	RMSE	Mean	$Q_{2.5\%}$	$\mathrm{Q}_{97.5\%}$	RMSE		
α_1 joint α_2 joint	$0.50 \\ 0.80$	$0.44 \\ 0.79$	$-0.42 \\ 0.47$	1.29 1.10	$0.36 \\ 0.15$	0.48 0.84	$-0.10 \\ 0.61$	1.24 1.02	$0.31 \\ 0.15$		
α_3 joint	1.00	0.98	0.40	1.56	0.24	1.38	0.69	1.62	0.43		
β_1 joint β_2 joint β_3 joint	-0.30 -0.40 -0.20	-0.16 -0.23 -0.02	-0.34 -0.52 -0.29	$0.02 \\ 0.06 \\ 0.25$	0.17 0.26 0.21	$ \begin{array}{r r} -0.28 \\ -0.36 \\ -0.18 \end{array} $	-0.34 -0.73 -0.25	-0.12 -0.06 0.19	0.07 0.11 0.09		
σ_1^2 joint σ_2^2 joint σ_3^2 joint	1.00 0.50 0.30	$0.97 \\ 0.46 \\ 0.37$	0.62 0.32 0.22	1.48 0.66 0.58	$0.19 \\ 0.09 \\ 0.12$	0.92 0.35 0.25	$0.69 \\ 0.24 \\ 0.14$	1.21 0.51 0.42	0.17 0.19 0.09		
$ \rho_1 \text{ joint} $ $ \rho_2 \text{ joint} $ $ \rho_3 \text{ joint} $	4.00 3.00 2.00	5.55 3.72 5.38	2.46 1.69 2.01	10.92 7.42 12.76	2.12 1.68 5.53	5.03 4.57 2.82	3.14 2.14 1.27	7.73 8.93 18.79	1.26 2.52 1.05		
a_1 joint a_2 joint a_3 joint	0.40 0.50 0.60	$0.33 \\ 0.45 \\ 0.76$	-0.24 0.02 0.35	0.79 0.75 0.95	$0.26 \\ 0.24 \\ 0.20$	0.45 0.47 0.58	0.13 0.04 0.14	$0.70 \\ 0.82 \\ 0.97$	0.14 0.37 0.20		

identify in this setting, likely due to the fact that when gridded covariates are missing, the latent fields lose large-scale structure, which might lead to the overestimation of ρ .

Finally, the temporal coefficients a_1 , a_2 , and a_3 remain relatively stable between the two simulation studies. The posteriors and RMSEs change only slightly when gridded covariates are added in the joint model, suggesting inference in the joint model is dominated by the point data.

4. Real data application

Soil moisture is important for hydrology, agriculture, and climate (Entekhabi et al., 1996; Seneviratne et al., 2010), and monitoring it is vital for drought and flood management, irrigation planning, and improving climate models. Yet making accurate, consistent maps over large areas is challenging. We map soil moisture in the Elliot Water catchment by combining sparse but accurate SEPA in-situ measurements with the wide coverage of Copernicus satellite data. By fusing point and gridded data, we produce fine-resolution maps with quantified uncertainty, leveraging sensor accuracy and satellite spatio-temporal coverage. We apply the models in Equation (12) and (13) to data from the Scottish Environment Protection Agency (SEPA)¹, Copernicus² and the Open

¹https://www2.sepa.org.uk/sensornet

²https://land.copernicus.eu/global/products/ssm

Elevation³. We define three variables according to our real soil moisture data: y_1 : rainfall (spatially misaligned covariate), y_2 : soil temperature (spatially aligned covariate), y_3 : volumetric water content (VWC, response variable) and x: elevation (the fixed effect). The in-situ monitoring network includes 10 rainfall gauges and 22 soil stations that report soil temperature and moisture. The satellite provides estimates of the soil water index (SWI), a quantity related to VWC. SWI is a derived Copernicus product (Copernicus Land Monitoring Service, 2024), available on a daily basis at 1 km resolution, corresponding to a 5×19 grid over our study catchment. The real data application incorporates multiple days of soil moisture data, allowing for the evaluation of temporal information in prediction modelling. By including data from multiple time points, the spatio-temporal data fusion model aims to determine whether modelling temporal dependencies alongside spatial correlation leads to better predictive performance on the real datasets. Specifically, the temporal information enables the model to potentially use patterns such as soil moisture persistence, seasonal effects, or delayed responses to covariates (rainfall). This section aims to quantify the gains in prediction accuracy from the incorporation of temporal structure, thereby providing insights into the advantages of spatio-temporal modelling for soil moisture data fusion.

Figure 3 presents the one-day-ahead prediction map based on a 10-day training set from 06/05/2022 to 15/05/2022. We construct a standardised water index by standardising in-situ VWC measurements and satellite SWI values so that they are on a common scale. It is noted that the gridded covariates of the satellite data are missing, so the only available gridded data is the response variable. It displays the raw observations, the 95% prediction interval, and the mean predictions for the point model, grid model and joint model. It reveals that the spatial pattern is strongly dominated by elevation in the point model, the grid model captures more spatial detail due to its broader spatial coverage, and the joint model, which integrates both point and gridded data, narrows the CIs of the prediction by using the strengths of both datasets.

Table 3 and 4 show the posterior means along with the 95% credible intervals (2.5% and 97.5% quantiles) for the spatio-temporal model with different numbers of time points (t=3 and t=10). The number of time points corresponds to using data from t days before the prediction date (16/05/2022). The parameters are grouped into intercepts, scaling parameters, spatial parameters, and temporal coefficients. Each parameter is evaluated across three models (joint, point, and grid) within the spatio-temporal model framework, with the model fitted for time points of t=3 and t=10. The intercept estimates across the point grid and the joint model vary, and for most of the intercepts, there is less uncertainty with t=10 than with t=3. The scaling parameters suggest that the effects are different between t=3 and t=10, with the exception that θ_1 remains negative across both values of t, which is plausible as soil temperature or rainfall patterns likely changed between these time points. The range (ρ) and variance (σ) also vary a lot, and the temporal coefficients (a_3) indicate strong temporal autocorrelation for y_3 .

The real data application reveals a trade-off between temporal autocorrelation and parameter uncertainty in the spatio-temporal model. While increasing the number of time points (t = 10) improves precision for parameters with strong temporal persistence (e.g., coefficients like a_3), it increases uncertainty for intercepts (α_3) . The conflict reflects

³https://open-elevation.com

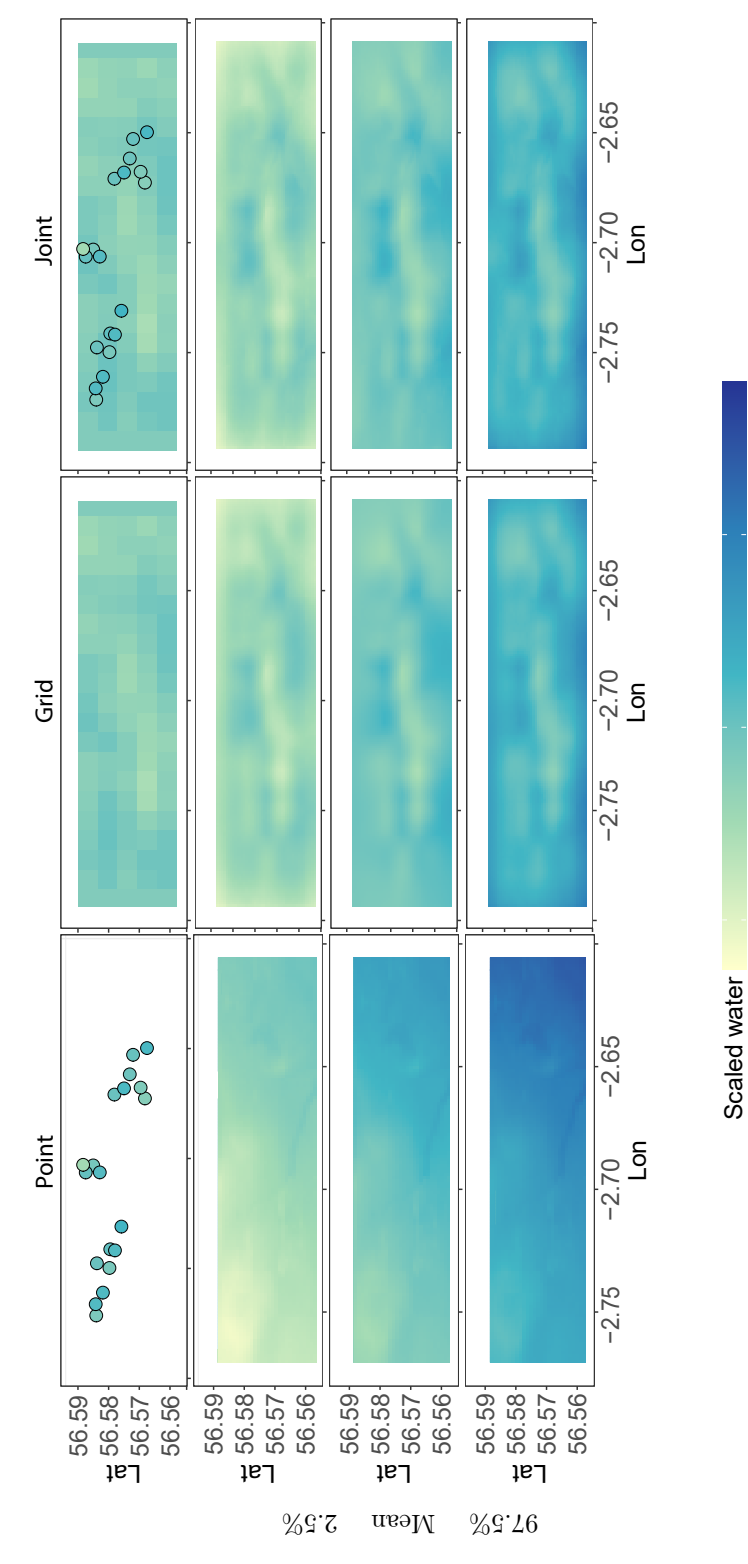


Figure 3: Prediction maps of the standardised water index (computed from VWC and SWI) over the Elliott water catchment area on 16/05/2022 (the 10-day training set includes data from 06/05/2022 to 15/05/2022), using the same mesh, with 95% confidence intervals. The top row displays the real data for each model, while the subsequent rows show the 95% prediction interval, including the 2.5% and 97.5% quantiles as well as the mean of the predictions.

0

2

index

Table 4: Parameter estimates with posterior means and 95% CIs, obtained by fitting the point, grid and joint spatio-temporal data fusion models to the soil moisture data.

(a) Intercepts

Param	t=3	t = 10
α_1 point α_1 joint	$ \begin{vmatrix} -0.55 (-0.59, -0.51) \\ -0.55 (-0.59, -0.51) \end{vmatrix} $	$ \begin{vmatrix} -0.29 (-0.42, -0.16) \\ -0.30 (-0.63, 0.02) \end{vmatrix} $
α_2 point α_2 joint	$ \begin{vmatrix} 0.12 (-0.34, 0.58) \\ 0.18 (-1.07, 1.42) \end{vmatrix} $	$ \begin{array}{c c} 0.02 (-0.18, 0.22) \\ 0.12 (-0.17, 0.42) \end{array} $
$ \alpha_3 \text{ point} \alpha_3 \text{ grid} \alpha_3 \text{ joint} $	$ \begin{vmatrix} 0.33 (-0.92, 1.58) \\ 0.42 (-3.90, 4.75) \\ 0.29 (-4.18, 4.76) \end{vmatrix} $	$ \begin{array}{c} 0.33 (-4.30, 4.96) \\ 0.22 (-7.53, 7.98) \\ 0.17 (-7.88, 8.22) \end{array} $
	(b) Scaling parame	ters
β_1 point β_1 joint	$ \begin{array}{c c} 0.01 \ (-0.55, \ 0.58) \\ -0.05 \ (-0.50, \ 0.39) \end{array} $	0.11 (-0.40, 0.66) 2.51 (2.18, 2.83)
β_2 point β_2 joint	$ \begin{array}{c c} -0.07 (-0.35, 0.22) \\ -0.81 (-1.28, -0.33) \end{array} $	0.27 (0.15, 0.38) 0.60 (0.38, 0.85)
θ_1 point θ_1 grid θ_1 joint	$ \begin{vmatrix} -1.70 & (-2.18, -1.22) \\ -0.31 & (-0.59, -0.04) \\ -0.85 & (-1.06, -0.63) \end{vmatrix} $	$ \begin{array}{c c} -1.18 (-1.38, -0.98) \\ -0.14 (-0.52, 0.24) \\ -0.35 (-0.52, -0.17) \end{array} $
	(c) Spatial parameters (varian	nce and range)
σ_1^2 point σ_1^2 joint	0.02 (0.01, 0.05) 0.03 (0.01, 0.07)	0.11 (0.05, 0.20) 1.31 (0.78, 2.07)
σ_2^2 point σ_2^2 joint	0.92 (0.61, 1.30) 0.92 (0.41, 1.82)	0.93 (0.80, 1.09) 0.98 (0.80, 1.18)
σ_3^2 point σ_3^2 grid σ_3^2 joint	1.13 (0.73, 1.69) 2.84 (2.05, 3.87) 2.89 (2.09, 3.91)	0.33 (0.12, 0.67) 3.09 (2.44, 3.87) 3.13 (2.47, 3.92)
$ \rho_1 \text{ point} \\ \rho_1 \text{ joint} $	$\begin{array}{c c} 3.6 \times 10^4 \left(1.1 \times 10^4, 9.8 \times 10^4\right) \\ 4.2 \times 10^4 \left(1.3 \times 10^4, 1.2 \times 10^5\right) \end{array}$	$\begin{array}{ c c c c c c }\hline & 4.3 \times 10^4 \left(2.0 \times 10^4, 9.1 \times 10^4\right) \\ & 2.1 \times 10^4 \left(1.5 \times 10^4, 2.8 \times 10^4\right) \\ \hline\end{array}$
$ \rho_2 \text{ point} \rho_2 \text{ joint} $	$\begin{array}{ c c c c }\hline 1.8 \times 10^3 \left(6.0 \times 10^2, 4.3 \times 10^3\right) \\ 8.1 \times 10^3 \left(2.9 \times 10^3, 1.9 \times 10^4\right)\end{array}$	$\begin{array}{c} 9.2 \times 10^{2} \left(6.1 \times 10^{2}, 1.3 \times 10^{3}\right) \\ 3.5 \times 10^{3} \left(2.6 \times 10^{3}, 4.7 \times 10^{3}\right) \end{array}$
$ \rho_3 \text{ point} $ $ \rho_3 \text{ grid} $ $ \rho_3 \text{ joint} $	$ \begin{array}{c c} 7.8 \times 10^3 \left(3.5 \times 10^3, 1.5 \times 10^4 \right) \\ 9.1 \times 10^3 \left(7.5 \times 10^3, 1.1 \times 10^4 \right) \\ 6.2 \times 10^3 \left(4.6 \times 10^3, 8.4 \times 10^3 \right) \end{array} $	$ \begin{array}{c c} 8.3 \times 10^4 \left(3.7 \times 10^4, 1.8 \times 10^5 \right) \\ 1.1 \times 10^4 \left(8.7 \times 10^3, 1.3 \times 10^4 \right) \\ 1.1 \times 10^4 \left(8.7 \times 10^3, 1.3 \times 10^4 \right) \end{array} $

Table 4: Parameter estimates with posterior means and 95% credible intervals (2.5% and 97.5% quantiles), obtained by fitting the point, grid and joint spatio-temporal data-fusion models to the soil moisture data. (continued)

(d) Temporal coefficient parameters

Param	t=3	t=10
a_1 point a_1 joint	0.36 (-0.51, 0.92) 0.53 (-0.46, 0.99)	0.33 (-0.20, 0.78) 0.98 (0.94, 0.99)
a_2 point a_2 joint	0.09 (-0.33, 0.48) 0.46 (-0.43, 0.94)	0.07 (-0.09, 0.23) -0.22 (-0.51, 0.07)
a_3 point a_3 grid a_3 joint	0.05 (-0.51, 0.60) 0.98 (0.97, 0.99) 0.98 (0.97, 0.99)	0.92 (0.73, 0.99) 0.98 (0.97, 0.99) 0.98 (0.97, 0.99)

model structural constraints introduced by more time points (sparse daily point data, weak identifiability or stronger spatio-temporal interactions). The spatial range may vary over time, but the current model assumes it is fixed. For weakly identified parameters (e.g., β_1 and β_2), additional time points lead to unstable parameter estimation, while strongly autocorrelated temporal processes ($a_3 \approx 1$) benefited from more time points. The results highlight the importance of balancing model complexity with data adequacy: more temporal data improves signals for dominant processes but increases noise in hierarchical parameters, which needs careful prior specification or model redesign to stabilise inferences.

It is noted that increasing the time points does not guarantee decreasing the uncertainty for all parameters. Adding more time points provides more repeated measures over time, which contributes to the estimation of the temporal coefficients by capturing long-term patterns and reduces the uncertainty of the parameter estimation (e.g., narrower CIs for temporal coefficients a_k). In Table 4, the a_1 of the joint model at t=10 has a posterior mean with a tight interval compared to t=3, where the CIs are wider. For example, when t=3, the temporal coefficient a_1 from the joint model is estimated at 0.53 with a 95% CI of (-0.46, 0.99), whereas for t=10, it increases to 0.98 with a narrower CI of (0.94, 0.99). This indicates that the certainty in the temporal coefficients improves as the number of time points increases in the model. In Table 4c, uncertainty does not always decrease with more time points. The estimation of ρ_3 varies and its intervals widen, whereas intervals for ρ_1 and ρ_2 tighten. This instability for ρ_3 likely reflects the nonstationarity for the process, so the assumption of the same daily range may be inappropriate.

5. Discussion and conclusions

We develop a spatio-temporal data fusion model for point and gridded data, building upon the spatial framework of Moraga et al. (2017) and its spatio-temporal extension by He and Wong (2024). However, the latter's model framework treats covariates only as fixed effects, so misaligned covariates cannot be accommodated in the framework. We address this issue by modelling selected covariates as individual latent spatio-temporal

fields and mapping both responses and covariates to observation supports via aggregation operators. With arbitrary point and areal supports, it explicitly handles misaligned covariates and responses, and also allows different measurement errors for point sensors and gridded data. Key structures include a latent Gaussian random field with Matérn spatial covariance extended over time via an AR(1), and a fusion strategy that integrates point sensor data and gridded satellite data under a separable spatio-temporal dependence. It makes it possible to model the environmental process from both spatial and temporal dimensions because such processes change continuously across space and through time. The spatio-temporal data fusion model is fitted using the INLA-SPDE approach for fast inference and prediction. The model assumes that the point and gridded data come from the same latent field with trend covariates, and point and gridded data are mapped using the projection matrix in the SPDE.

The simulations study the effects of t on prediction and parameter estimation, robustness under missing gridded covariates, and differences between point and grid model specifications. The model is robust to gridded covariates' missingness, and performance is almost unchanged. Across point, grid, and joint models evaluated at $t \in \{3,7,10\}$, increasing t generally improves the parameter estimation and prediction: RMSE decreases for $\alpha_1, \alpha_2, \beta_1, \beta_2$ (e.g., the RMSE of β_1 drops by 35% from t = 3 to t = 10), and credible intervals narrow. The joint model consistently outperforms the point and grid model by about 15-20% in RMSEs for scaling parameters and 10-15% for spatial variances at t=10. Some biases still exist (especially in α_3 and ρ_3), indicating sensitivity to modelling assumptions such as separable covariance, fixed smoothness, and the over-simplified AR(1) temporal structure. The joint model's robustness highlights the importance of spatio-temporal frameworks in complex systems with evolving spatial patterns. Overall, incorporating multiple time points improves predictive performance and enhances the accuracy and stability of parameter estimation. In particular, increasing the time points from t=3 to t=10 narrows CIs and reduces bias for fixed effects and hyperparameters because temporal replication at the same locations adds information about the latent process and measurement noise.

The spatio-temporal model improves both parameter estimation and prediction. Increasing the time points from t=3 to t=10 narrows CIs and reduces bias for fixed effects and hyperparameters, because temporal replication at the same locations adds information about the latent process and measurement noise.

In the real data application, predicted mean surfaces remain smooth far from sensors. With a sparse network, the model borrows strength from covariates. Elevation is available everywhere and explains large-scale variation, so uncertainty widens where there is little nearby sensor support. The contrast between t=3 and t=10 shows a trade-off: adding time points improves estimates and predicts even without new sensor data, but temporal replication cannot fully compensate for limited spatial coverage, and fine-scale detail still needs more locations or gridded data.

Future work can be improved in several directions. Firstly, relaxing the model structure. In particular, moving beyond separable spatio-temporal covariances (e.g., non-separable covariance or SPDEs with time varying coefficients), allows spatially varying and possibly varying ranges (treat $\rho(\mathbf{s})$ as covariate dependent or as a random field), and generalises the temporal process from AR(1) to more flexible forms such as AR(p) or ARMA. Secondly, temporal misalignment should be incorporated in a unified way. The model could be extended to handle irregular temporal sampling and different temporal

support for the point and gridded data. Thirdly, future work should systematically assess robustness to irregular sampling by evaluating performance under spatial and temporal irregularity (e.g., long gaps, informative missingness) via blocked spatio-temporal cross-validation. Finally, data quality is very important, as the current monitoring network in the real data is sparse and unevenly distributed, optimised placement of the sensors, together with additional covariates, is expected to improve the identifiability of (ρ, σ^2) and reduce bias.

Acknowledgements

We thank Armando Marino and Claire Neil for helpful discussions and for providing us with soil moisture data. This paper has been prepared using the European Union's Copernicus Land Monitoring Service information https://land.copernicus.eu/global/products/ssm and the in-situ sensor data from Scottish Environment Protection Agency (SEPA) https://www2.sepa.org.uk/sensornet. W. Zheng acknowledges funding from the Chinese Scholarship Council and the fee waiver from the University of Glasgow.

Code

The code used for the simulation study and real data application in the paper is publicly available at STDF-COSP on GitHub.

Appendix A. Appendix 1: Additional details about the simulation study

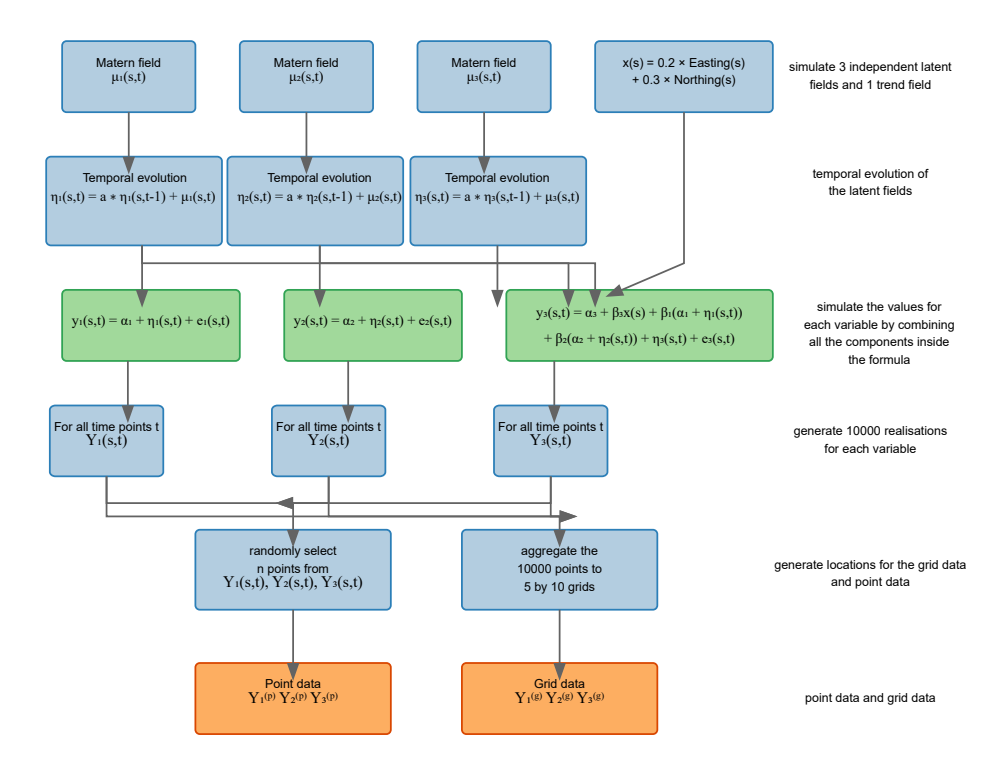


Figure A.4: Flowchart illustrating the simulation process for the spatio-temporal study. The first row shows the generation of independent latent fields for each variable. The second row introduces temporal dependence. The third row combines these components into a full spatio-temporal realisation. Subsequent rows demonstrate how gridded data and point data are derived from this realisation.

- 1. Spatial processes $\mu(s)$ are simulated by generating 100 independent random field realisations from a Matérn Gaussian random field as fixed seeds, and the same 100 seeds are reused when constructing datasets of length t days. Holding the spatial field fixed over time makes sure that differences across scenarios arise from t, not from spatial variability. The behaviour of the Matérn Gaussian field is controlled through three parameters within the Matérn covariance function: range (ρ) , marginal variance (σ) , and smoothness (v).
- 2. The temporal correlation is introduced by the formula as follows:

$$\eta(s,t) = a * \eta(s,t-1) + \sqrt{1-a^2} * \mu(s,t),$$

where the $\sqrt{1-a^2}$ term is used to make the process stationary in time. The spatiotemporal process is assumed to be a series of GRFs, and the latent spatial processes $\mu_k(s)$ generated from the first step account for the temporal dependencies through AR(1).

Table A.5: True parameter values used in the spatio-temporal simulation data

	α_1	α_2	α_3	β_1	β_2	θ_1	ρ_1	ρ_2	ρ_3	σ_1	σ_2	σ_3	$ au_{p1}^2$	$ au_{p2}^2$	$ au_{p3}^2$	$ au_{g1}^2$	$ au_{g2}^2$	$ au_{g3}^2$	a_1	a_2	a_3
True values	0.5	0.8	1	-0.3	-0.4	-0.2	4	3	2	1	0.5	0.3	0.09	0.04	0.01	0.25	0.16	0.09	0.4	0.5	0.6

3. The trend covariate x(s,t), which represents the geological trend of the study catchment, is derived from a surface where values exhibit an increasing pattern from the southwest to the northeast (from 0 to 3.5) across the whole study catchment. Let the coordinates of $y(s_i,t)$ be denoted by Easting_i and Northing_i, then the trend is defined as follows:

$$x(s_i, t) = 0.2 * \text{Easting}_i + 0.3 * \text{Northing}_i$$
(A.1)

- 4. The uncorrected measurement error terms for point data (e_p) and gridded data (e_g) are generated from a Gaussian white-noise process: $N(0, \tau_p^2)$ and $N(0, \tau_q^2)$.
- 5. Then the covariates and the response variables are generated by combining the previously constructed terms based on Equations (12) and (13). Table A.5 shows the true parameters used in the spatio-temporal simulation study. The parameters for the simulation study are chosen based on both previous studies and real data characteristics to make sure that they are both theoretically reliable and practically feasible. Some parameters, such as the intercepts α and precision parameters τ , are borrowed from previous studies to maintain comparison with other models. Others, such as scaling parameters β , spatial parameters ρ and σ , and the temporal coefficients a, are chosen from real data applications to reflect spatial patterns and characteristics in the real soil moisture dataset. This allows the simulation to balance theoretical evidence with real data conditions, which makes the assessment of the model's performance meaningful.
- 6. The gridded data is generated by first simulating independent realisations of a Matérn Gaussian random field to model the latent fields. Then, for each time point, values for gridded cells are calculated by averaging all points within that cell to ensure that each gridded cell represents the localised mean of the specific latent field. The process can be defined as: $Y^{(g)}(\mathbf{B}) = \frac{1}{n} \sum_{i=1}^{n} y_i$, where $Y^{(g)}(\mathbf{B})$ represents the average value of the gridded cell, which indicates the mean of all values y_i within the gridded cell, n denotes the total number of points within the gridded cell \mathbf{B} , and y_i represents the value of the ith points within the gridded cell in each day.
- 7. To assess the model's ability to generalise unobserved data, the test set includes 20 randomly selected unobserved point locations for the response variable y_3 on the final day of the training period and one day ahead of the training period, with test points always at the same locations across the point model, grid model and joint mode within each simulation. Randomly selecting test locations across different simulations gives a comprehensive evaluation of the model's out-of-sample performance, reducing potential bias and assessing how well the fusion model predicts at unobserved locations.

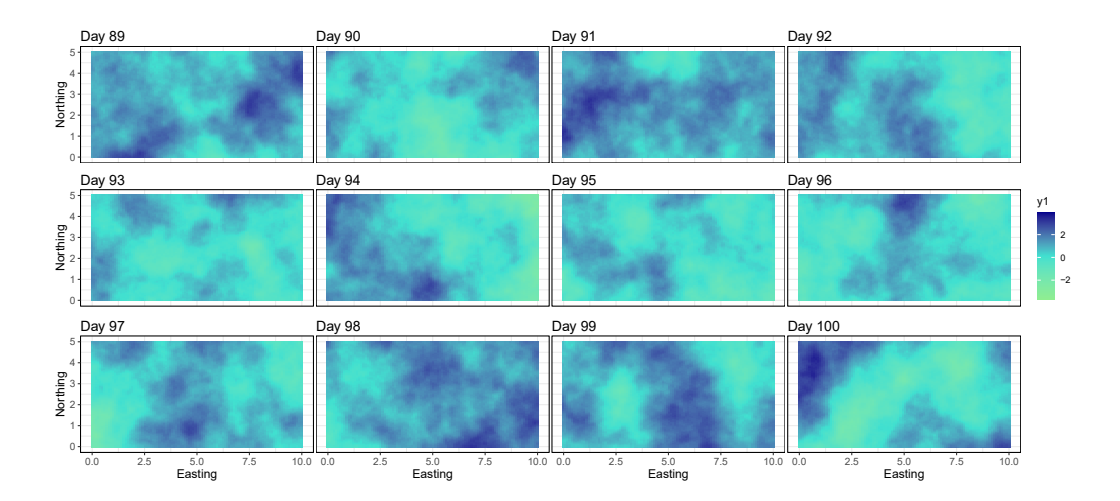


Figure A.5: Final 12-day sequence of simulated latent fields for simulated rainfall y_1 in the spatiotemporal simulation study, using a latent field configuration ($\sigma_1 = 1$, $\sigma_2 = 0.5$, $\sigma_3 = 0.3$) and a temporal coefficient $a_1 = 0.4$.

This section characterises the spatio-temporal simulation data used in the spatiotemporal simulation study, which provides insight into how spatial patterns evolve over time.

The latent field η_3 simulates soil moisture dynamics using a spatially continuous and temporally autoregressive dependence structure. The spatial field is modelled as a Gaussian process with a Matérn covariance (smoothness $\rho_3 = 2$, variance $\sigma_3 = 0.1$), and the temporal dynamics as an AR(1) process with coefficients $a_1 = 0.4$, $a_2 = 0.5$, and $a_3 = 0.6$ corresponding to rainfall, soil moisture, and VWC, respectively. The autoregressive parameters are chosen based on the exploratory analysis of the real sensor data, which reflects the characteristics of the real data. The simulation fields span over a 5 × 10 spatial domain and evolve over 100 simulated time points, but only the final 12 are shown here.

Both the point data and grid data, along with the latent fields, are simulated by the models (12) and (13) according to the workflow in Figure A.4. The sensor network is simulated by sampling 22 locations across all time points. At each time point, we sample 10,000 values to evaluate the Matérn Gaussian random field, and average the values within each grid cell to approximate the spatial integral. After the independent daily data are generated, the AR(1) process is used to introduce the temporal dependence across time into the data.

The point data include a measurement error denoted as τ_{p_3} . In contrast, the grid data includes a measurement error denoted as τ_{g_3} , with τ_{g_3} being greater than τ_{p_3} because the sensor data is considered to be more accurate. This indicates that the grid data has greater measurement uncertainty compared to the point data, which aligns with the real-world data characteristic, where sensor data are generally more accurate than satellite image data.

Figure A.5, A.6 and A.7 demonstrate how the latent fields change across space and

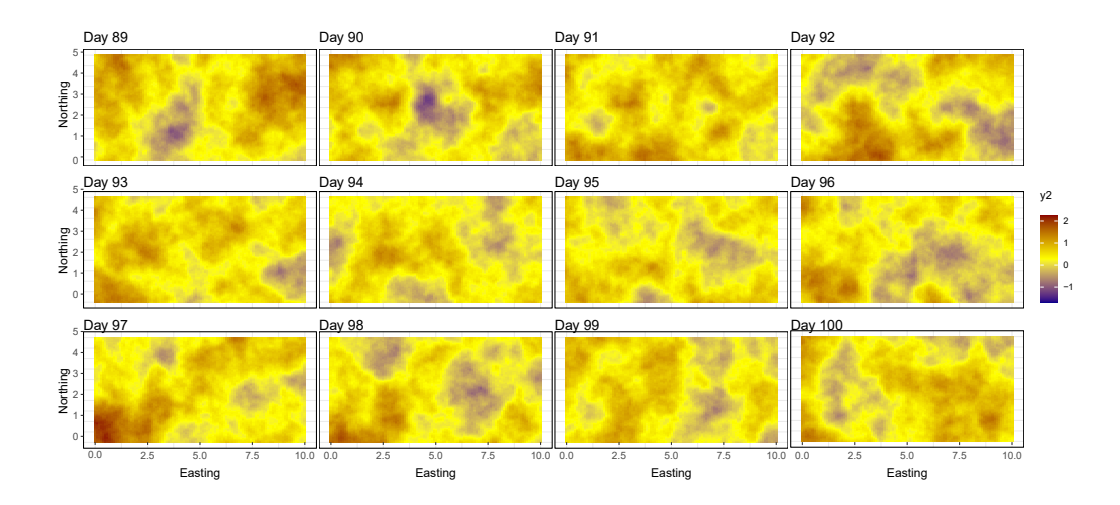


Figure A.6: Final 12-day sequence of simulated latent fields for simulated soil temperature y_2 in the spatio-temporal simulation study, using a latent field configuration ($\sigma_1 = 1$, $\sigma_2 = 0.5$, $\sigma_3 = 0.3$) and a temporal coefficient $a_2 = 0.5$.

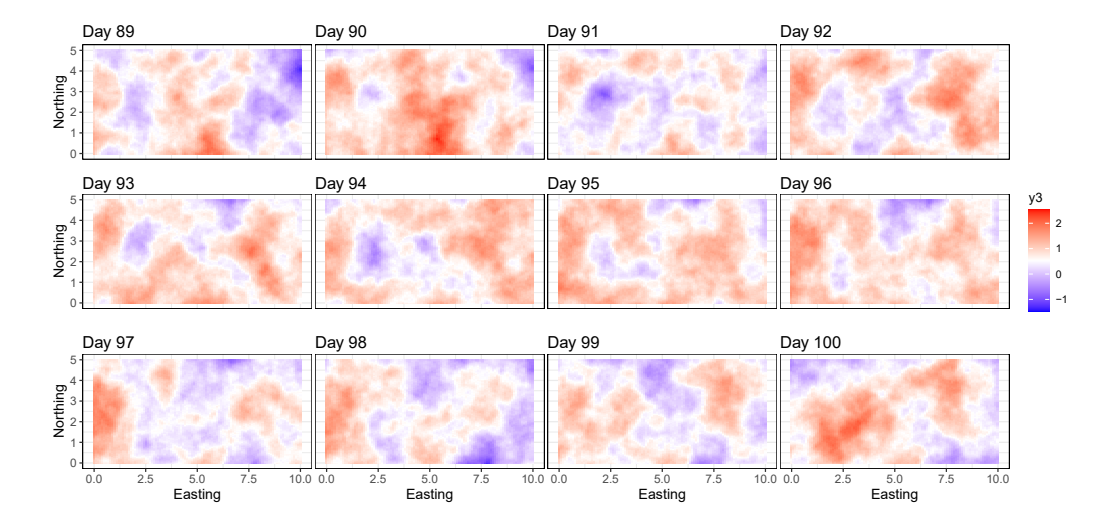


Figure A.7: Final 12-day sequence of simulated latent fields for simulated soil moisture y_3 in the spatiotemporal simulation study, using a latent field configuration ($\sigma_1 = 1$, $\sigma_2 = 0.5$, $\sigma_3 = 0.3$) and a temporal coefficient $a_3 = 0.6$.

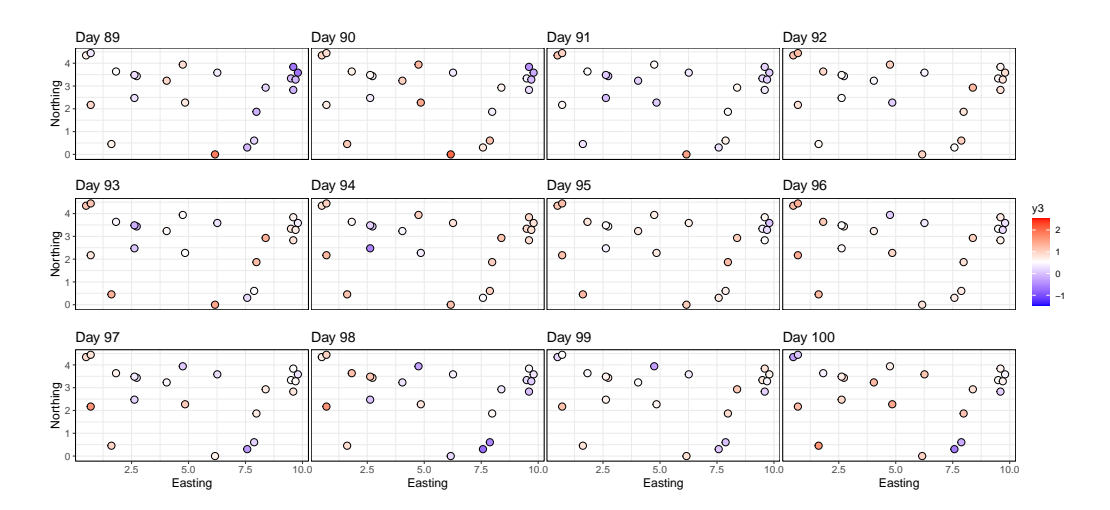


Figure A.8: Final 12-day of simulated point soil moisture data for y_3 in the spatio-temporal simulation study. Twenty-two points are randomly selected from the realisation surface of simulated soil moisture y_3 on each day.

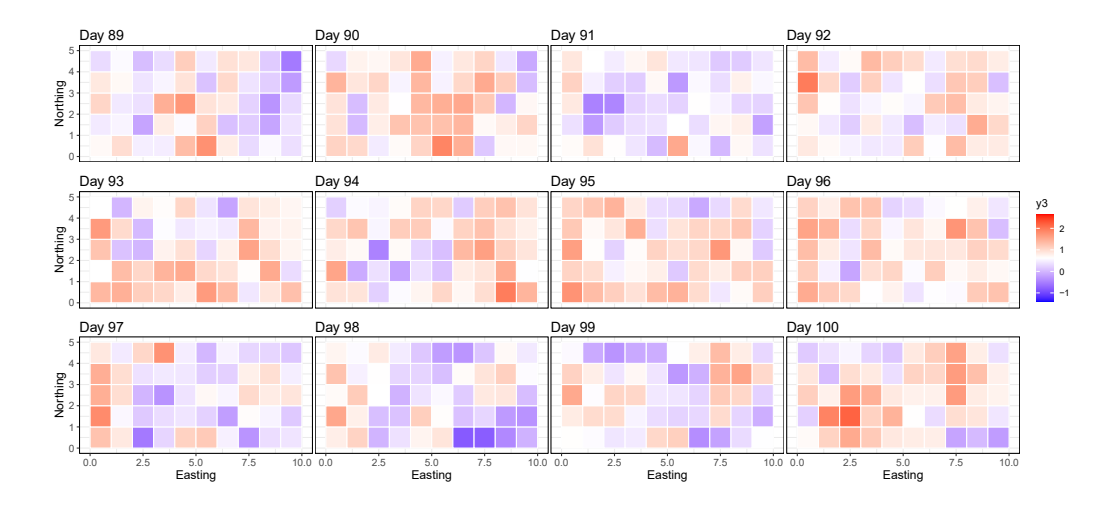


Figure A.9: Final 12-day of simulated grid soil moisture data for y_3 in the spatio-temporal simulation study. It is averaged by 10,000 points generated from the realisation surface of simulated soil moisture y_3 on each day.

Table A.6: Prior specification for the temporal coefficient in the spatio-temporal data fusion model.

Param	Informative prior	Non-informative prior
α_1		N(0,10)
α_2		N(0,10)
α_3		N(0,10)
eta_1		N(0,10)
eta_2		N(0,10)
$ heta_1$		N(0,10)
$ ho_1$	$PC(\rho_0, \alpha)$	
$ ho_2$	$PC(\rho_0, \alpha)$	
$ ho_3$	$PC(\rho_0, \alpha)$	
σ_1^2	$PC(\sigma_0, \alpha)$	
σ_2^2	$PC(\sigma_0, \alpha)$	
σ_3^2	$PC(\sigma_0, \alpha)$	
$\sigma_{e_1}^2$		$\mathrm{PC}\left(au_{e_1}, lpha ight)$
$\sigma_{e_2}^2$		$\mathrm{PC}\left(au_{e_2}, lpha ight)$
σ_{11}^{2} σ_{22}^{2} σ_{33}^{2} $\sigma_{e_{11}}^{2}$ $\sigma_{e_{22}}^{2}$ $\sigma_{e_{33}}^{2}$ $\sigma_{e_{11}}^{2}$ $\sigma_{e_{22}}^{2}$ $\sigma_{e_{33}}^{2}$ $\sigma_{e_{43}}^{2}$		$\mathrm{PC}\left(au_{e_3}, lpha ight)$
$\sigma_{e_1}^2$		$\mathrm{PC}\left(au_{e_1}, lpha ight)$
$\sigma_{e_2}^2$		$\mathrm{PC}\left(au_{e_2}, lpha\right)$
$\sigma_{e_3}^2$		$\mathrm{PC}\left(au_{e_3}, lpha ight)$
a_1		$PC(0.5, \alpha)$
a_2		$PC(0.5, \alpha)$
a_3		$PC(0.5, \alpha)$

over time. Figure A.8 shows the spatial distribution of sparse sensor locations, and Figure A.9 shows the coarse-resolution satellite data covering the whole study catchment. The autoregressive coefficients of each variable are $a_1=0.4$, $a_2=0.5$ and $a_3=0.6$ respectively, which is quite moderate temporal dependence, so the spatial pattern across different time points is not very obvious. Since the point data and grid data are a combination of all three latent fields $(\mu_1, \mu_2, \text{ and } \mu_3)$, it is even challenging to tell the temporal trends in the point data and grid data figures.

The prior distributions' parameters in the spatio-only and spatio-temporal model, such as intercepts, scaling parameters, and spatial parameters, are the same as those used in the spatio-only model, except for the temporal coefficients, whose priors are specified separately in Table A.6. The penalised-complexity (PC) priors are used here for the temporal coefficients to guide the Bayesian inference process towards less complex solutions by penalising complexity and the distance from the base model by shrinking the range toward infinity and the marginal variance toward zero (Fuglstad et al., 2019).

References

Berrocal, V.J., Gelfand, A.E., Holland, D.M., 2012. Space-time data fusion under error in computer model output: an application to modeling air quality. Biometrics 68, 837–848.

- Cameletti, M., Gómez-Rubio, V., Blangiardo, M., 2019. Bayesian modelling for spatially misaligned health and air pollution data through the inla-spde approach. Spatial Statistics 31, 100353.
- Cameletti, M., Lindgren, F., Simpson, D., Rue, H., 2013. Spatio-temporal modeling of particulate matter concentration through the spde approach. AStA Advances in Statistical Analysis 97, 109–131.
- Copernicus Land Monitoring Service, 2024. Soil moisture. URL: https://land.copernicus.eu/en/products/soil-moisture.accessed: 2024-11-11.
- Cressie, N., Wikle, C.K., 2015. Statistics for spatio-temporal data. John Wiley & Sons.
- Entekhabi, D., Rodriguez-Iturbe, I., Castelli, F., 1996. Mutual interaction of soil moisture state and atmospheric processes. Journal of Hydrology 184, 3–17.
- Forlani, C., Bhatt, S., Cameletti, M., Krainski, E., Blangiardo, M., 2020. A joint bayesian space—time model to integrate spatially misaligned air pollution data in r-inla. Environmetrics 31, e2644.
- Fuentes, M., Raftery, A.E., 2005. Model evaluation and spatial interpolation by bayesian combination of observations with outputs from numerical models. Biometrics 61, 36–45.
- Fuglstad, G.A., Simpson, D., Lindgren, F., Rue, H., 2019. Constructing priors that penalize the complexity of gaussian random fields. Journal of the American Statistical Association 114, 445–452.
- Gelfand, A.E., Zhu, L., Carlin, B.P., 2001. On the change of support problem for spatiotemporal data. Biostatistics 2, 31–45.
- Gotway, C.A., Young, L.J., 2002. Combining incompatible spatial data. Journal of the American Statistical Association 97, 632–648.
- Gotway, C.A., Young, L.J., 2007. A geostatistical approach to linking geographically aggregated data from different sources. Journal of Computational and Graphical Statistics 16, 115–135.
- Gryparis, A., Paciorek, C.J., Zeka, A., Schwartz, J., Coull, B.A., 2009. Measurement error caused by spatial misalignment in environmental epidemiology. Biostatistics 10, 258–274.
- He, S., Wong, S.W., 2024. Spatio-temporal data fusion for the analysis of in situ and remote sensing data using the inla-spde approach. Spatial Statistics 64, 100863.
- Krainski, E., Gómez-Rubio, V., Bakka, H., Lenzi, A., Castro-Camilo, D., Simpson, D., Lindgren, F., Rue, H., 2018. Advanced spatial modeling with stochastic partial differential equations using R and INLA. Chapman and Hall/CRC.
- Lindgren, F., Rue, H., 2015. Bayesian spatial modelling with r-inla. Journal of statistical software 63, 1–25.

- Lindgren, F., Rue, H., Lindström, J., 2011. An explicit link between gaussian fields and gaussian markov random fields: the stochastic partial differential equation approach. Journal of the Royal Statistical Society: Series B (Statistical Methodology) 73, 423–498.
- Madsen, L., Ruppert, D., Altman, N.S., 2008. Regression with spatially misaligned data. Environmetrics: The official journal of the International Environmetrics Society 19, 453–467.
- McMillan, N.J., Holland, D.M., Morara, M., Feng, J., 2010. Combining numerical model output and particulate data using bayesian space—time modeling. Environmetrics: The official journal of the International Environmetrics Society 21, 48–65.
- Moraga, P., Cramb, S.M., Mengersen, K.L., Pagano, M., 2017. A geostatistical model for combined analysis of point-level and area-level data using inla and spde. Spatial Statistics 21, 27–41.
- Nguyen, H., Cressie, N., Braverman, A., 2012. Spatial statistical data fusion for remote sensing applications. Journal of the American Statistical Association 107, 1004–1018.
- Pouliot, G.A., 2023. Spatial econometrics for misaligned data. Journal of Econometrics 232, 168–190.
- Rue, H., Martino, S., Chopin, N., 2009. Approximate bayesian inference for latent gaussian models by using integrated nested laplace approximations. Journal of the royal statistical society: Series b (statistical methodology) 71, 319–392.
- Sahu, S.K., Gelfand, A.E., Holland, D.M., 2010. Fusing point and areal level space—time data with application to wet deposition. Journal of the Royal Statistical Society Series C: Applied Statistics 59, 77–103.
- Scott, E.M., 2023. Framing data science, analytics and statistics around the digital earth concept. Environmetrics 34, e2732.
- Seneviratne, S.I., Corti, T., Davin, E.L., Hirschi, M., Jaeger, E.B., Lehner, I., Orlowsky, B., Teuling, A.J., 2010. Investigating soil moisture-climate interactions in a changing climate: A review. Earth-Science Reviews 99, 125–161.
- Suen, M.H., Naylor, M., Lindgren, F., 2025. Cohering disaggregation and uncertainty quantification for spatially misaligned data. arXiv preprint arXiv:2502.10584.
- Szpiro, A.A., Sheppard, L., Lumley, T., 2011. Efficient measurement error correction with spatially misaligned data. Biostatistics 12, 610–623.
- Villejo, S.J., Martino, S., Lindgren, F., Illian, J.B., 2025. A data fusion model for meteorological data using the inla-spde method. Journal of the Royal Statistical Society Series C: Applied Statistics, qlaf012.
- Wang, C., Furrer, R., 2019. Combining heterogeneous spatial datasets with process-based spatial fusion models: A unifying framework. arXiv preprint arXiv:1906.00364 .

- Wikle, C.K., Berliner, L.M., 2005. Combining information across spatial scales. Technometrics 47, 80–91.
- Wilkie, C., Miller, C., Scott, E., O'Donnell, R., 2019. Nonparametric statistical down-scaling for the fusion of data of different spatiotemporal support. Environmetrics 30, e2549.
- Wilson, K., Wakefield, J., 2020. Pointless spatial modeling. Biostatistics 21, e17–e32.
- Zheng, W., Elliott, A., Miller, C., Scott, M., 2024. Spatial regression with misaligned covariates for soil moisture mapping, Durham University, Durham, UK. pp. 329–331. URL: https://durham-repository.worktribe.com/output/2741031. conference dates: 14–19 July 2024.
- Zhong, R., Moraga, P., 2023. Bayesian hierarchical models for the combination of spatially misaligned data: a comparison of melding and downscaler approaches using inla and spde. Journal of Agricultural, Biological and Environmental Statistics, 1–20.